SIAM J. SCI. COMPUT.
Vol. 42, No. 5, pp. A2620–A2654

STABILIZED CUT DISCONTINUOUS GALERKIN METHODS FOR ADVECTION-REACTION PROBLEMS*

CEREN GÜRKAN†, SIMON STICKO‡, AND ANDRÉ MASSING‡§

Abstract. We develop novel stabilized cut discontinuous Galerkin methods for advection-reaction problems. The domain of interest is embedded into a structured, unfitted background mesh in $\mathbb{R}^d$ where the domain boundary can cut through the mesh in an arbitrary fashion. To cope with robustness problems caused by small cut elements, we introduce ghost penalties in the vicinity of the embedded boundary to stabilize certain (semi-)norms associated with the advection and reaction operator. A few abstract assumptions on the ghost penalties are identified enabling us to derive geometrically robust and optimal a priori error and condition number estimates for the stationary advection-reaction problem which hold irrespective of the particular cut configuration. Possible realizations of suitable ghost penalties are discussed. The theoretical results are corroborated by a number of computational studies for various approximation orders and for two- and three-dimensional test problems.

Key words. advection-reaction problems, discontinuous Galerkin, cut finite element method, stabilization, a priori error estimates, condition number

AMS subject classifications. 65N30, 65N12, 65N85

DOI. 10.1137/18M1206461

1. Introduction.

To ease the burden of mesh generation in finite element based simulation pipelines, novel so-called unfitted finite element methods have gained much attention in recent years; see [12] for a recent overview. In unfitted finite element methods, the mesh is exonerated from the task to represent the domain geometry accurately and used only to define proper approximation spaces. The geometry of the model domain is described independently by means of a separate geometry model, e.g., a CAD or level set based description, or even another, independently generated tessellation of the geometry boundary. Combined with suitable techniques to properly impose boundary or interface conditions, for instance, by means of Lagrange multipliers or Nitsche type methods [51, 36, 20, 21, 94, 98, 10], complex geometries can be simply embedded into an easy-to-generate background mesh. Alternative routes to impose boundary and interface conditions for embedded geometries are taken in the immersed finite element method [80, 79] and in finite element based formulations of the immersed boundary method [11].

As the embedded geometry can cut arbitrarily through the background mesh, a main challenge is to devise unfitted finite element methods that are *geometrically robust* in the sense that a priori error and condition number estimates hold with constants independent of the particular cut configuration. One possible solution to achieve geometrical robustness is provided by the approach taken in the *cut finite*

*Submitted to the journal's Methods and Algorithms for Scientific Computing section August 14, 2018; accepted for publication (in revised form) April 28, 2020; published electronically September 9, 2020.
https://doi.org/10.1137/18M1206461
Funding: This work was funded by the Kempe Foundation under Postdoc Scholarship JCK-1612 and by the Swedish Research Council under Starting Grant 2017-05038.
†Department of Civil Engineering, Kadir Has University, Cibali, 34083 Fatih, Istanbul, Turkey (ceren.gurkan@khas.edu.tr).
‡Department of Mathematics and Mathematical Statistics, Umeå University, SE-90187 Umeå, Sweden (andre.masssing@umu.se, simon.sticko@umu.se).
§Department of Mathematical Sciences, Norwegian University of Science and Technology, NO-7491 Trondheim, Norway (andre.massing@ntnu.no).

element method (CutFEM) [24], which is based on a theoretically founded stabilization framework. The CutFEM stabilization technique allows one to transfer stability and approximation properties from a finite element scheme posed on a standard mesh to its cut finite element counterpart. As a result, a wide range of problem classes has been treated including, e.g., elliptic interface problems [28, 59, 19], Stokes and Navier–Stokes type problems [22, 85, 17, 29, 86, 105, 72, 53, 58], and two-phase and fluid-structure interaction problems [100, 55, 56, 84]. As a natural application area, unfitted finite element methods have also been proposed for problems in fractured porous media [44, 48, 37, 45].

In addition to the aforementioned unfitted *continuous* finite element methods, unfitted *discontinuous Galerkin* (DG) methods have been successfully devised to treat boundary and interface problems on complex and evolving domains [5, 6, 97], including flow problems with moving boundaries and interfaces [103, 65, 96, 88, 74, 75]. In contrast to stabilized continuous CutFEMs, in unfitted DG methods, troublesome small cut elements can be merged with neighbor elements with a large intersection support by simply extending the local shape functions from the large element to the small cut element. As interelement continuity is enforced only weakly, no additional measures need to be taken to force the modified basis functions to be globally continuous. Consequently, cell merging in unfitted DG methods provides an alternative stabilization mechanism to ensure that the discrete systems are well-posed and well-conditioned. For a very recent extension of the cell merging approach to continuous finite elements, we refer to [4]. Thanks to their favorable conservation and stability properties, unfitted DG methods remain an attractive alternative to continuous CutFEMs, but some drawbacks are the almost complete absence of numerical analysis except for [87, 70], the required rather invasive implementational changes in standard DG assembly and solving routines to account for cell merging, and the lack of natural discretization approaches for PDEs defined on surfaces.

Starting with the early contributions [30, 93], cell merging has also been a popular approach to mitigate small cut cell related stability issues and severe time-step restrictions in explicit time-stepping methods for finite volume based Cartesian cut cell discretizations of compressible flow problems [64, 99], and hyperbolic conservation laws in general. For cut cell methods based on balancing numerical fluxes, a major challenge is the robustness of the cell merging process, in particular for complex three-dimensional (3D) geometries or for problems with moving boundaries [8]. Alternative approaches exist, such as the h-box method [66, 9] and stabilized fluxes in dimensionally split methods [73, 52], but the resulting formulations are typically of at most second order. For an overview of Cartesian cut cell methods and approaches to overcome small cut cell related problems, we refer to the recent review [8].

So far, most of the theoretically analyzed unfitted finite element schemes have been proposed for elliptic type problems. In contrast to conducted research on finite volume based Cartesian cut cell methods, very little attention has been paid to the theoretical development of unfitted finite element methods for advection-dominant or hyperbolic problems, except for [86, 105], which consider a continuous interior penalty (CIP) based CutFEM for the Oseen problem, and [27, 90, 26], which develop continuous unfitted finite element methods for advection-diffusion equations on surfaces based on the CIP and streamline upwind Petrov–Galerkin approach. On the other hand, for the DG community, hyperbolic problems have been of interest from the very beginning, as the first DG method was developed by [95] to model the neutron transport problem. The first analysis of these methods was presented in [77] and then improved in [71], while [13] reformulated and generalized the upwind flux strategy in

DG methods for hyperbolic problems by introducing a tunable penalty parameter. The advantageous conservation and stability properties, the high locality, and the naturally inherited upwind flux term in the bilinear form make DG methods popular to handle specifically advection dominated problems [31, 69, 106] as well as elliptic ones [3, 43]. For a detailed overview, we refer to the monographs [38, 67], which include comprehensive bibliographies on DG methods for both elliptic and hyperbolic problems.

1.1. Novel contributions and outline of this paper. In this work we continue the development of a novel *stabilized* cut discontinuous Galerkin (CutDG) framework initiated in [57]. Departing from the elliptic boundary and interface problems considered in [57], we here propose and analyze CutDG methods for scalar, first-order hyperbolic problems. The main focus is profoundly on stationary problems, but we shall briefly demonstrate that the same type of method also extends to time-dependent problems. However, the analysis of the time-dependent case is postponed to future work. The proposed methods do not rely on the cell merging methodology; instead geometrical robustness is achieved by adding properly designed ghost penalty stabilization in the vicinity of the embedded boundary. The idea of extending ghost penalty stabilization techniques from the continuous CutFEM approach [16] to DG-based discretizations allows for a minimally invasive extension of existing fitted DG software to handle unfitted geometries. Only additional quadrature routines need to be added to handle the numerical integration on cut geometries, and we refer to the numerous quadrature algorithms capable of higher-order geometry approximation [89, 97, 76, 47, 46] which have been proposed in recent years. With a suitable choice of the ghost penalty, the sparsity pattern of the matrix associated with the advection-reaction operator requires little manipulation compared to its fitted DG counterpart. In fact, the resulting stencil on elements near the embedded boundary will correspond to the stencil of a symmetric interior penalty method [2] for second-order diffusion problems which in many DG-based finite element libraries is already readily available. But similar to the cell merging approach, our stabilization framework works automatically for higher-order approximation spaces with polynomial orders p and is not limited to low-order schemes.

We start by briefly recalling the advection-reaction model problems and the corresponding weak formulations in section 2, followed by the presentation of the stabilized CutDG methods in section 3, which includes additional abstract ghost penalties. A main feature of the presented numerical analysis is that we identify a number of abstract assumptions on the ghost penalty to prove geometrically robust optimal a priori error and condition number estimates which hold independent of the particular cut configuration. To prepare the a priori error analysis, section 4 collects a number of useful inequalities and explains the construction of an unfitted but stable L^2 projection operator. In section 5, we derive an inf-sup condition in a ghost penalty enhanced scaled streamline diffusion type norm. A key observation is that the classical argument in [13] based on boundedness on orthogonal subscales does not work as the local orthogonality properties of the unfitted L^2 projection are perturbed due to the mismatch between the physical domain and the active mesh where the discontinuous ansatz functions are defined. In section 6, the results from the previous sections are combined to establish an optimal a priori error estimate of the form $\mathcal{O}(h^{p+1/2})$ for the proposed stationary CutDG method with constants independent of the particular cut configuration. We continue our abstract analysis in section 7 and prove that the condition number of the matrix related to the advection-reaction operator scales like

$\mathcal{O}(h^{-1})$, again with geometrically robust constants. To the best of our knowledge, this is the first time a theoretical analysis of any type of unfitted DG method for an advection-reaction problem is presented. Our theoretical investigation concludes by discussing a number of ghost penalty realizations in section 8. In section 9, we briefly demonstrate how the ghost penalty approach can be combined with explicit Runge–Kutta methods to solve the time-dependent advection-reaction problem under a standard hyperbolic CFL condition. Finally, we corroborate our theoretical analysis with numerical examples in section 10, where we study both the convergence properties and the geometrical robustness of the proposed CutDG method.

1.2. Basic notation. Throughout this work, $\Omega \subset \mathbb{R}^d$, $d = 2, 3$, denotes an open and bounded domain with piecewise smooth boundary $\partial\Omega$, while $\Gamma = \partial\Omega$ denotes its topological boundary. For $U \in \{\Omega, \Gamma\}$ and $0 \leqslant m < \infty$, $1 \leqslant q \leqslant \infty$, let $W^{m,q}(U)$ be the standard Sobolev spaces consisting of those $\mathbb{R}$-valued functions defined on U which possess L^q-integrable weak derivatives up to order m. Their associated norms are denoted by $\|\cdot\|_{m,q,U}$. As usual, we write $H^m(U) = W^{m,2}(U)$ and $(\cdot,\cdot)_{m,U}$ and $\|\cdot\|_{m,U}$ for the associated inner product and norm. If unmistakable, we occasionally write $(\cdot,\cdot)_U$ and $\|\cdot\|_U$ for the inner products and norms associated with $L^2(U)$, with U being a measurable subset of $\mathbb{R}^d$. Any norm $\|\cdot\|_{\mathcal{P}_h}$ used in this work which involves a collection of geometric entities $\mathcal{P}_h$ should be understood as a broken norm defined by $\|\cdot\|^2_{\mathcal{P}_h} = \sum_{P\in\mathcal{P}_h} \|\cdot\|^2_P$ whenever $\|\cdot\|_P$ is well-defined, with a similar convention for scalar products $(\cdot,\cdot)_{\mathcal{P}_h}$. Any set operation involving $\mathcal{P}_h$ is also understood as an elementwise operation, e.g., $\mathcal{P}_h \cap U = \{P \cap U \mid P \in \mathcal{P}_h\}$ and $\partial\mathcal{P}_h = \{\partial P \mid P \in \mathcal{P}_h\}$, allowing for compact shorthand notation such as $(v,w)_{\mathcal{P}_h\cap U} = \sum_{P\in\mathcal{P}_h}(v,w)_{P\cap U}$ and $\|\cdot\|_{\partial\mathcal{P}_h\cap U} = \sqrt{\sum_{P\in\mathcal{P}_h}\|\cdot\|^2_{\partial P\cap U}}$. Finally, throughout this work, we use the notation $a \lesssim b$ for $a \leqslant Cb$ for some generic constant C (even for $C = 1$) which varies with the context but is always independent of the mesh size h and the position of Γ relative to the background $\mathcal{T}_h$ but may depend on the dimensions d, the polynomial degree of the finite element functions, the shape regularity of the mesh, and the curvature of Γ.

2. Model problems. For a given vector field $b \in [W^{1,\infty}(\Omega)]^d$ and a scalar function $c \in L^\infty(\Omega)$ we consider the advection-reaction problem of the form

$$b \cdot \nabla u + cu = f \quad \text{in } \Omega, \tag{2.1a}$$

$$u = g \quad \text{on } \Gamma^-, \tag{2.1b}$$

where $g \in L^2(\Gamma^-)$ describes the boundary value on the inflow boundary of Ω defined by

$$\Gamma^- = \{x \in \partial\Omega \mid b(x) \cdot n_\Gamma(x) < 0\}. \tag{2.2}$$

Here, n_Γ denotes the outer normal associated with Γ. Correspondingly, the outflow and characteristic boundary are defined by, respectively,

$$\Gamma^+ = \{x \in \partial\Omega \mid b(x) \cdot n_\Gamma(x) > 0\}, \tag{2.3}$$

$$\Gamma^0 = \{x \in \partial\Omega \mid b(x) \cdot n_\Gamma(x) = 0\}. \tag{2.4}$$

As usual in this setting, we assume that

$$c_0 \coloneqq \operatorname*{ess\,inf}_{x\in\Omega} \left(c(x) - \frac{1}{2}\nabla\cdot b(x) \right) > 0. \tag{2.5}$$

The corresponding weak formulation of scalar hyperbolic problem (2.1) is to seek $u \in V \coloneqq \{v \in L^2(\Omega) \mid b \cdot \nabla v \in L^2(\Omega)\}$ such that $\forall\, v \in V$

$$a(u, v) = l(v), \tag{2.6}$$

with the bilinear form $a(\cdot, \cdot)$ and linear form $l(\cdot)$ given by

$$a(u, v) = (b \cdot \nabla u + cu, v)_\Omega - (b \cdot n_\Gamma u, v)_{\Gamma^-}, \qquad l(v) = (f, v)_\Omega - (b \cdot n_\Gamma g, v)_{\Gamma^-}. \tag{2.7}$$

As we briefly consider time-dependent problems, we shall also solve

$$\partial_t u + b \cdot \nabla u + cu = f \quad \text{in } \Omega, \tag{2.8a}$$
$$u = g \quad \text{on } \Gamma^-, \tag{2.8b}$$
$$u|_{t=0} = u_0 \quad \text{in } \Omega. \tag{2.8c}$$

The weak form corresponding to (2.8) reads, Find u so that for each fixed $t \in (0, T)$, $u \in V$ and such that u fulfills

$$(\partial_t u, v)_\Omega + a(u, v) = l(v) \quad \forall\, v \in V, \tag{2.9a}$$
$$u|_{t=0} = u_0. \tag{2.9b}$$

3. Cut discontinuous Galerkin methods for advection-reaction problems. Let $\widetilde{\mathcal{T}}_h$ be a background mesh covering $\overline{\Omega}$ consisting of d-dimensional, shape-regular (closed) polygons, $\{T\}$, which are either simplices or quadrilaterals/hexahedrals. As usual, we introduce the local mesh size $h_T = \operatorname{diam}(T)$ and the global mesh size $h = \max_{T \in \widetilde{\mathcal{T}}_h}\{h_T\}$. For $\widetilde{\mathcal{T}}_h$ we define the so-called active mesh,

$$\mathcal{T}_h = \{T \in \widetilde{\mathcal{T}}_h \mid T \cap \Omega^\circ \neq \emptyset\}, \tag{3.1}$$

and its submesh $\mathcal{T}_\Gamma$ consisting of all elements cut by the boundary,

$$\mathcal{T}_\Gamma = \{T \in \mathcal{T}_h \mid T \cap \Gamma \neq \emptyset\}. \tag{3.2}$$

Note that since the elements $\{T\}$ are closed by definition, the active mesh $\mathcal{T}_h$ still covers Ω. The set of interior faces in the active background mesh is given by

$$\mathcal{F}_h = \{F = T^+ \cap T^- \mid T^+, T^- \in \mathcal{T}_h \;\wedge\; T^+ \neq T^-\}. \tag{3.3}$$

To keep the technical details in the forthcoming numerical analysis at a moderate level, we make two reasonable geometric assumptions on $\mathcal{T}_h$ and Γ.

Assumption G1. The mesh $\mathcal{T}_h$ is quasi-uniform.

Assumption G2. For $T \in \mathcal{T}_\Gamma$ there is an element T' in $\omega(T)$ with a "fat" intersection such that

$$|T' \cap \Omega|_d \geqslant c_s |T'|_d \tag{3.4}$$

for some mesh independent $c_s > 0$. Here, $\omega(T)$ denotes the set of elements sharing at least one node with T.

Remark 3.1. Quasi-uniformity of $\mathcal{T}_h$ is assumed mostly for notational convenience. Except for the condition number estimates, all derived estimates can be easily localized to element or patchwise estimates.

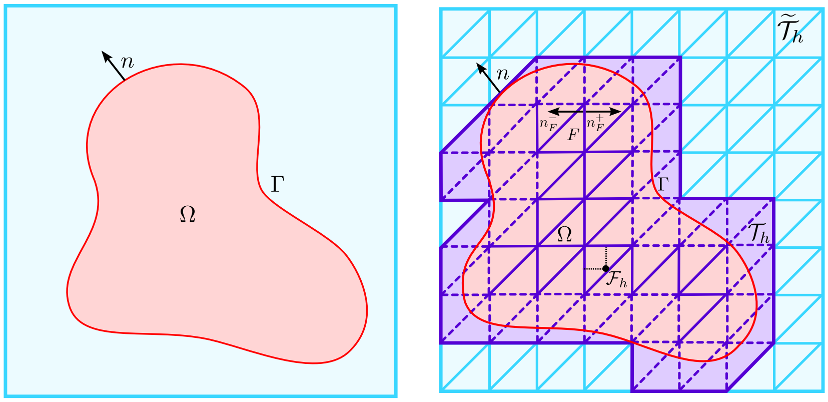

FIG. 3.1. *Computational domains for problems* (2.1) *and* (2.8). *(Left) Physical domain* Ω *with boundary* Γ *and outer normal* n. *(Right) Background mesh and active mesh used to define the approximation space. Dashed faces are used to define face-based ghost penalties discussed in section* 8.

Remark 3.2. The "fat" intersection property guarantees that Γ is reasonably resolved by the active mesh $\mathcal{T}_h$. It is automatically satisfied if, e.g., $\Gamma \in C^2$ and h is small enough, that is, if $h \lesssim \min_{\{1,\dots,d-1\}} \|\frac{1}{\kappa_i}\|_{L^\infty(\Gamma)}$, where $\{\kappa_1, \dots, \kappa_{d-1}\}$ are the principal curvatures of Γ; see [19].

On the active mesh $\mathcal{T}_h$, we define the discrete function space V_h as the broken polynomial space of order p,

$$V_h \coloneqq \mathbb{P}_p(\mathcal{T}_h) \coloneqq \bigoplus_{T \in \mathcal{T}_h} \mathbb{P}_p(T). \tag{3.5}$$

To formulate our CutDG discretization of the weak problem (2.6), we recall the usual definitions of the averages

$$\{\sigma\}|_F = \frac{1}{2}(\sigma_F^+ + \sigma_F^-), \tag{3.6}$$

$$\{n_F \cdot \sigma\}|_F = \frac{1}{2} n_F \cdot (\sigma_F^+ + \sigma_F^-), \tag{3.7}$$

and the jump across an interior facet $F \in \mathcal{F}_h$,

$$[w]|_F = w_F^+ - w_F^-. \tag{3.8}$$

Here, $w_F^{\pm}(x) = \lim_{t \to 0^+} w(x \mp t n_F)$ for some chosen unit facet normal n_F on F.

Remark 3.3. To keep the notation at a moderate level, we will from here on drop any subscripts indicating whether a normal belongs to a face F or to the boundary Γ as it will be clear from the context.

With these definitions in place, our CutDG method for advection-reaction problem (2.1) can be formulated as follows, Find $u_h \in V_h$ such that $\forall\, v \in V_h$

$$A_h(u_h, v) \coloneqq a_h(u_h, v) + g_h(u_h, v) = l_h(v). \tag{3.9}$$

The discrete bilinear forms $a_h(\cdot,\cdot)$ and $l_h(\cdot)$ represent the classical discrete, DG counterparts of (2.6) defined on mesh elements and faces restricted to the physical domain Ω. More precisely, for $v, w \in V_h$, we let

$$a_h(v,w) = (b\cdot\nabla v + cv, w)_{\mathcal{T}_h\cap\Omega} - (b\cdot nv, w)_{\Gamma^-}$$
$$- (b\cdot n[v], \{w\})_{\mathcal{F}_h\cap\Omega} + \frac{1}{2}(|b\cdot n|[v],[w])_{\mathcal{F}_h\cap\Omega}, \tag{3.10}$$
$$l_h(w) = (f,w)_\Omega - (b\cdot ng, w)_{\Gamma^-}. \tag{3.11}$$

The main difference to the classical DG method for problem (2.1) (cf. [13, 38]) is the appearance of an additional stabilization form g_h, also known as a *ghost penalty*. The role of the ghost penalty is to ensure that the favorable stability and approximation properties of the classical upwind stabilized DG method carry over to the unfitted mesh scenario. The precise requirements on g_h will be formulated as a result of the theoretical analysis performed in the remaining sections, but we already point out that since problem (2.1) involves an advection and a reaction term, it will be natural to assume that g_h can be decomposed in a reaction related ghost penalty g_c and an advection related ghost penalty g_b, both of which we assume to be symmetric,

$$g_h(v,w) = g_c(v,w) + g_b(v,w) \quad \forall\, v,w\in V_h. \tag{3.12}$$

In the same manner, the CutDG method for the time-dependent problem (2.8) reads, Find u_h such that for each fixed $t\in(0,T)$, $u_h\in V_h$ and

$$M_h(\partial_t u_h, v) + A_h(u_h,v) = l_h(v) \quad \forall v\in V_h, \tag{3.13a}$$
$$u_h|_{t=0} = \pi_{M_h}u_0. \tag{3.13b}$$

Here, M_h denotes the stabilized $L^2(\Omega)$ inner product,

$$M_h(v,w) = (v,w)_\Omega + g_m(v,w), \quad v,w\in V_h, \tag{3.14}$$

where the only difference between g_m and g_c is a scaling by c_0:

$$g_c(v,w) = c_0 g_m(v,w), \quad v,w\in V_h. \tag{3.15}$$

In (3.13b), $\pi_{M_h}: L^2(\Omega)\to V_h$ denotes the stabilized L^2 projection. This projection is defined as the solution to the problem, Find $\pi_{M_h}u = \tilde{u}_h\in V_h$ such that

$$M_h(\tilde{u}_h, v) = (u,v)_\Omega \quad \forall v\in V_h. \tag{3.16}$$

Remark 3.4. For the sake of simplicity, we shall in the following sections restrict the analysis to the case when the mesh consists of simplices. We also restrict the analysis to the method (3.9) for the stationary problem (2.1), since this is our main focus. However, in section 10.3 we shall by numerical experiments verify that the method (3.13) works for the time-dependent problem (2.8) using quadrilaterals.

4. Norms, useful inequalities, and approximation properties. Following the presentation in [38], we introduce a reference velocity b_c and a reference time τ_c,

$$b_c = \|b\|_{0,\infty,\Omega}, \qquad \tau_c^{-1} = \|c\|_{0,\infty,\Omega} + |b|_{1,\infty,\Omega}, \tag{4.1}$$

and define the central flux, upwind, and the scaled streamline diffusion norm by setting

$$|||v|||_{\mathrm{cf}}^2 = \tau_c^{-1}\|v\|_\Omega^2 + \frac{1}{2}\||b\cdot n|^{1/2}v\|_\Gamma^2, \tag{4.2}$$
$$|||v|||_{\mathrm{up}}^2 = |||v|||_{\mathrm{cf}}^2 + \frac{1}{2}\||b\cdot n|^{1/2}[v]\|_{\mathcal{F}_h\cap\Omega}^2, \tag{4.3}$$
$$|||v|||_{\mathrm{sd}}^2 = |||v|||_{\mathrm{up}}^2 + \|\phi_b^{1/2} b\cdot\nabla v\|_{\mathcal{T}_h\cap\Omega}^2, \tag{4.4}$$

respectively. Thanks to the assumed quasi-uniformity, the global scaling factor ϕ_b is given by

$$\phi_b = h/b_c. \tag{4.5}$$

For each norm $|||\cdot|||_t$ with $t \in \{\mathrm{cf}, \mathrm{up}, \mathrm{sd}\}$, its ghost penalty enhanced version is given by

$$|||v|||_{t,h}^2 = |||v|||_t^2 + |v|_{g_h}^2. \tag{4.6}$$

To simplify a number of estimates, we will also use a slightly stronger norm than $|||\cdot|||_{\mathrm{sd},h}$, namely

$$|||v|||_{\mathrm{sd},h,*}^2 = |||v|||_{\mathrm{cf}}^2 + \|\phi_b^{1/2} b\cdot\nabla v\|_{\mathcal{T}_h\cap\Omega}^2 + b_c\|v\|_{\partial\mathcal{T}_h\cap\Omega}^2 + |v|_{g_h}^2. \tag{4.7}$$

Finally, we assume as in [38] that the mesh $\mathcal{T}_h$ is sufficiently resolved such that the inequality

$$h \leqslant b_c\tau_c \tag{4.8}$$

is satisfied, which means that problem (2.1) can be considered as advection dominant on the element level and that the advective velocity field b is sufficiently resolved in the sense that the following estimates hold:

$$\|c\|_{0,\infty,\Omega} h \leqslant b_c, \qquad |b|_{1,\infty,\Omega} \leqslant \frac{b_c}{h}. \tag{4.9}$$

Before we turn to the stability and a priori error analysis in section 5, we briefly review some useful inequalities needed later and explain how a suitable approximation operator can be constructed on the active mesh $\mathcal{T}_h$. Recall that for $v \in H^1(\mathcal{T}_h)$, the local trace inequalities of the form

$$\|v\|_{\partial T} \lesssim h^{-1/2}\|v\|_T + h^{1/2}\|\nabla v\|_T \quad \forall T \in \mathcal{T}_h, \tag{4.10}$$

$$\|v\|_{\Gamma\cap T} \lesssim h^{-1/2}\|v\|_T + h^{1/2}\|\nabla v\|_T \quad \forall T \in \mathcal{T}_h \tag{4.11}$$

hold; see [60] for a proof of the second one. For $v_h \in V_h$, let D^j be the jth total derivative; then the following inverse inequalities hold:

$$\|D^j v_h\|_{T\cap\Omega} \lesssim h^{i-j}\|D^i v_h\|_T \qquad \forall T \in \mathcal{T}_h, \quad 0 \leqslant i \leqslant j, \tag{4.12}$$

$$\|D^j v_h\|_{\partial T\cap\Omega} \lesssim h^{i-j-1/2}\|D^i v_h\|_T \quad \forall T \in \mathcal{T}_h, \quad 0 \leqslant i \leqslant j, \tag{4.13}$$

$$\|D^j v_h\|_{\Gamma\cap T} \lesssim h^{i-j-1/2}\|D^i v_h\|_T \quad \forall T \in \mathcal{T}_h, \quad 0 \leqslant i \leqslant j. \tag{4.14}$$

See [60] for a proof of the last one. Next, to define a suitable approximation operator, we depart from the L^2-orthogonal projection $\pi_h : L^2(\mathcal{T}_h) \to V_h$ which for $T \in \mathcal{T}_h$ and $F \in \mathcal{F}_T$ satisfies the error estimates

$$|v - \pi_h v|_{T,l} \lesssim h_T^{r-l}|v|_{r,T}, \qquad 0 \leqslant l \leqslant r, \tag{4.15}$$

$$|v - \pi_h v|_{F,l} \lesssim h_T^{r-l-1/2}|v|_{r,T}, \quad 0 \leqslant l \leqslant r - 1/2, \tag{4.16}$$

where $r \coloneqq \min\{s, p+1\}$ and whenever $v \in H^s(T)$. Now to lift a function $v \in H^s(\Omega)$ to $H^s(\Omega_h^e)$, where we for the moment use the notation $\Omega_h^e = \bigcup_{T\in\mathcal{T}_h} T$, we recall that for Sobolev spaces $W^{m,q}(\Omega)$, $0 < m \leqslant \infty, 1 \leqslant q \leqslant \infty$, there exists a bounded extension operator satisfying

$$(\cdot)^e : W^{m,q}(\Omega) \to W^{m,q}(\mathbb{R}^d), \quad \|v^e\|_{m,q,\mathbb{R}^d} \lesssim \|v\|_{m,q,\Omega} \tag{4.17}$$

for $u \in W^{m,q}(\Omega)$; see [104] for a proof. We can now define an unfitted L^2 projection variant $\pi_h^e : H^s(\Omega) \to V_h$ by setting

$$\pi_h^e v \coloneqq \pi_h v^e. \tag{4.18}$$

Note that this L^2 projection is slightly perturbed in the sense that it is orthogonal not on $L^2(\Omega)$ but rather on $L^2(\Omega_h^e)$. Combining the local approximation properties of π_h with the stability of the extension operator $(\cdot)^e$, we see immediately that π_h^e satisfies the global error estimates

$$\|v - \pi_h^e v\|_{\mathcal{T}_h,l} \lesssim h^{r-l}\|v\|_{r,\Omega}, \qquad 0 \leqslant l \leqslant r, \tag{4.19}$$

$$\|v - \pi_h^e v\|_{\mathcal{F}_h,l} \lesssim h^{r-l-1/2}\|v\|_{r,\Omega}, \quad 0 \leqslant l \leqslant r - 1/2, \tag{4.20}$$

$$\|v - \pi_h^e v\|_{\Gamma,l} \lesssim h^{r-l-1/2}\|v\|_{r,\Omega}, \quad 0 \leqslant l \leqslant r - 1/2. \tag{4.21}$$

Remark 4.1. It would have been possible to use the projection π_{M_h} from (3.16), instead of π_h^e, in the analysis of the method. This is done in, for example, [17]. However, using π_h^e will simplify the following analysis slightly.

Remark 4.2. In (4.19)–(4.21), we have intentionally neglected the superscript, e, on v and assumed that use of the extension operator, $(\cdot)^e$, is implied. In order to simplify the notation, we shall do so also in the following.

To ensure that the consistency error caused by g_h does not affect the convergence order, we require that the ghost penalties g_b and g_c are weakly consistent in the following sense.

Assumption HP1 (weak consistency estimate). For $u \in H^s(\Omega)$ and $r = \min\{s, p+1\}$, the seminorms $|\cdot|_{g_b}$ and $|\cdot|_{g_c}$ satisfy the estimates

$$|\pi_h^e u|_{g_b} \lesssim b_c^{1/2} h^{r-1/2}\|u\|_{r,\Omega}, \tag{4.22}$$

$$|\pi_h^e u|_{g_c} \lesssim \tau_c^{-1/2} h^r \|u\|_{r,\Omega}. \tag{4.23}$$

With these assumptions, the approximation error of the unfitted L^2 projection can be quantified with respect to the $|||\cdot|||_{\mathrm{sd},h,*}$ norm.

PROPOSITION 4.3. *Let $u \in H^s(\Omega)$ and assume that $V_h = \mathbb{P}_p(\mathcal{T}_h)$ with $p \geqslant 0$. Then for $r = \min\{s, p+1\}$, the approximation error of π_h^e satisfies*

$$|||u - \pi_h^e u|||_{\mathrm{sd},h,*} \lesssim (\tau_c^{-1/2} h^{1/2} + b_c^{1/2}) h^{r-1/2}\|u\|_{r,\Omega}. \tag{4.24}$$

Proof. Set $e_\pi = u - \pi_h^e u$; then by definition

$$|||e_\pi|||^2_{\mathrm{sd},h,*} = \tau_c^{-1}\|e_\pi\|^2_\Omega + \frac{1}{2}\||b\cdot n|^{1/2} e_\pi\|^2_\Gamma + b_c\|e_\pi\|^2_{\partial\mathcal{T}_h\cap\Omega} + \|\phi_b^{1/2} b\cdot\nabla e_\pi\|^2_\Omega + |e_\pi|^2_{g_h} \tag{4.25}$$

$$= I + II + III + IV + |e_\pi|^2_{g_h}. \tag{4.26}$$

Thanks to Assumption HP1, we only need to estimate I–IV. Using (4.19), I is bounded by

$$I \lesssim \tau_c^{-1} h^{2r}\|u\|^2_{r,\Omega}, \tag{4.27}$$

while the last three terms can be bounded by combining (4.19)–(4.21), leading to

$$II + III + IV \lesssim b_c\|h^{-1/2} e_\pi\|^2_{\mathcal{T}_h} + b_c\|h^{1/2}\nabla e_\pi\|^2_{\mathcal{T}_h} \lesssim b_c h^{2r-1}\|u\|^2_{r,\Omega}. \qquad \square \tag{4.28}$$

5. Stability analysis. The goal of this section is to show that the proposed stabilized CutDG method (3.9) satisfies a discrete inf-sup condition with respect to the $|||\cdot|||_{\mathrm{sd},h}$ norm, similar to the results presented in [40, 38] for the corresponding classical fitted DG method. In the unfitted case, one main challenge is that the proof of the inf-sup condition involves various inverse estimates, which in turn forces us to gain control over the considered $|||\cdot|||_{\mathrm{sd}}$ norm on the entire active mesh.

We start our theoretical analysis by recalling that a partial integration of the element contributions in the bilinear form (3.10) leads to a mathematically equivalent expression for a_h, namely,

$$a_h(v,w) = ((c-\nabla\cdot b)v,w)_{\mathcal{T}_h\cap\Omega} - (v, b\cdot\nabla w)_{\mathcal{T}_h\cap\Omega} + (b\cdot n v, w)_{\Gamma^+} + (b\cdot n\{v\},[w])_{\mathcal{F}_h\cap\Omega} + \frac{1}{2}(|b\cdot n|[v],[w])_{\mathcal{F}_h\cap\Omega}. \tag{5.1}$$

By taking the average of (3.10) and (5.1), we obtain the well-known decomposition of $a_h(\cdot,\cdot)$ into a symmetric and skew-symmetric part,

$$a_h(v,w) = a_h^{\mathrm{sy}}(v,w) + a_h^{\mathrm{sk}}(v,w), \tag{5.2}$$

where

$$a_h^{\mathrm{sy}}(v,w) = \left(\left(c - \frac{1}{2}\nabla\cdot b\right)v, w\right)_{\mathcal{T}_h\cap\Omega} + \frac{1}{2}(|b\cdot n|v,w)_\Gamma + \frac{1}{2}(|b\cdot n|[v],[w])_{\mathcal{F}_h\cap\Omega}, \tag{5.3}$$

$$a_h^{\mathrm{sk}}(v,w) = \frac{1}{2}\big((b\cdot\nabla v, w)_{\mathcal{T}_h\cap\Omega} - (v, b\cdot\nabla w)_{\mathcal{T}_h\cap\Omega} - (b\cdot n[v],\{w\})_{\mathcal{F}_h\cap\Omega} + (b\cdot n\{v\},[w])_{\mathcal{F}_h\cap\Omega}\big). \tag{5.4}$$

Consequently, the total bilinear form $A_h(\cdot,\cdot)$ is discretely coercive with respect to $|||\cdot|||_{\mathrm{up},h}$.

LEMMA 5.1. *For $v\in V_h$ it holds that*

$$c_0\tau_c |||v|||^2_{\mathrm{up},h} \lesssim A_h(v_h,v_h). \tag{5.5}$$

Proof. As in the classical fitted mesh case, the proof follows simply from observing that

$$A_h(v,v) = a_h(v,v) + g_h(v,v) = a_h^{\mathrm{sy}}(v,v) + g_h(v,v) \tag{5.6}$$

$$\geqslant c_0\|v\|^2_{\mathcal{T}_h\cap\Omega} + \frac{1}{2}\||b\cdot n|^{1/2}v\|^2_\Gamma + \frac{1}{2}\||b\cdot n|^{1/2}v\|^2_{\mathcal{F}_h\cap\Omega} + |v|^2_{g_h} \gtrsim c_0\tau_c|||v|||^2_{\mathrm{up},h}, \tag{5.7}$$

noting that $0 < c_0\tau_c \lesssim 1$ thanks to assumption (2.5) and the definition of τ_c; cf. (4.1). □

Remark 5.2. We point out that for the advection-reaction problem, the ghost penalty g_h is not needed to establish discrete coercivity in either the $|||\cdot|||_{\mathrm{up}}$ or the $|||\cdot|||_{\mathrm{up},h}$ norm, in contrast to the CutDG method for the Poisson problem presented in [57]. Nevertheless, we will see that g_h is required to prove an inf-sup condition for the discrete problem (3.9) using the stronger $|||\cdot|||_{\mathrm{sd},h}$ norm.

Following the derivation of the inf-sup condition in the fitted mesh case (see, for instance, [39]), a proper test function $v\in V_h$ needs to be constructed which establishes control over the streamline derivative. To construct such a suitable test function, we assume the existence of a discrete vector field $b_h^0 \in [\mathbb{P}_0(\mathcal{T}_h)]^d$ satisfying

$$\|b_h^0 - b\|_{0,\infty,T} \lesssim h_T |b|_{1,\infty,T}, \qquad \|b_h^0\|_{0,\infty,T} \lesssim \|b^e\|_{0,\infty,T}. \tag{5.8}$$

Note that for $b \in [W^{1,\infty}(\Omega)]^d$ such a discrete vector field b_h^0 can always be constructed. To establish the inf-sup result, the ghost penalties g_b and g_c for the discretized advection-reaction problem are supposed to satisfy the following assumptions.

Assumption HP2. The ghost penalty g_c extends the L^2 norm from the physical domain Ω to the active mesh in the sense that for $v_h \in V_h$, it holds that

$$\tau_c^{-1}\|v\|_{\mathcal{T}_h}^2 \lesssim \tau_c^{-1}\|v\|_{\Omega}^2 + |v|_{g_c}^2 \lesssim \tau_c^{-1}\|v\|_{\mathcal{T}_h}^2. \tag{5.9}$$

Assumption HP3. The ghost penalty g_b extends the streamline diffusion seminorm from the physical domain Ω to the active mesh in the sense that for $v_h \in V_h$, it holds that

$$\|\phi_b^{1/2} b\cdot\nabla v\|_{\mathcal{T}_h}^2 \lesssim \|\phi_b^{1/2} b\cdot\nabla v\|_{\Omega}^2 + |v|_{g_b}^2 + \tau_c^{-1}\|v\|_{\Omega}^2 + |v|_{g_c}^2 \lesssim \|\phi_b^{1/2} b\cdot\nabla v\|_{\mathcal{T}_h}^2 + \tau_c^{-1}\|v\|_{\mathcal{T}_h}^2. \tag{5.10}$$

Remark 5.3. At first it might be more natural to assume that

$$\|\phi_b^{1/2} b\cdot\nabla v\|_{\mathcal{T}_h}^2 \sim \|\phi_b^{1/2} b\cdot\nabla v\|_{\Omega}^2 + |v|_{g_b}^2 \tag{5.11}$$

is valid for $v \in V_h$ instead of the more convoluted estimate (5.10), but the forthcoming numerical analysis as well as the actual design of g_b will require us to frequently pass between certain locally constructed discrete vector fields b_h and the original vector field b. This is also the content of the next lemma.

LEMMA 5.4. *Let $v \in V_h$ and let $P \subset \mathcal{T}_h$ be an element patch with* $\operatorname{diam}(P) \sim h$. *Let b_h^P be a patchwise defined velocity field satisfying*

$$\|b_h^P - b\|_{0,\infty,P} \lesssim h|b^e|_{1,\infty,P}, \qquad \|b_h^P\|_{0,\infty,P} \lesssim \|b^e\|_{0,\infty,P}. \tag{5.12}$$

Then

$$\phi_b\|b_h^P - b\|_P^2\|\nabla v\|_P^2 \lesssim \tau_c^{-1}\|v\|_P^2. \tag{5.13}$$

Before we turn to the proof we note an immediate corollary of Lemma 5.4 and Assumption HP3.

COROLLARY 5.5. *Let $\mathcal{P}_h$ be a collection of patches and assume that the number of patch overlaps is uniformly bounded. Let b_h^P and $P \in \mathcal{P}_h$ satisfy the assumptions in Lemma* 5.4. *Then*

$$\|\phi_b^{1/2}(b_h^P - b)\cdot\nabla v\|_{\mathcal{P}_h}^2 \lesssim |||v|||_{\mathrm{up},h}^2. \tag{5.14}$$

Proof of Lemma 5.4. Thanks to the assumptions (5.12) and the fact that $\phi_b\|b\|_{0,\infty,P} \lesssim h$, we have the following chain of estimates:

$$\phi_b\|b_h - b\|_{0,\infty,P}^2 \lesssim \phi_b\|b\|_{0,\infty,P} h|b|_{1,\infty,P} \lesssim h^2|b|_{1,\infty,P}. \tag{5.15}$$

Thus an application of the Cauchy–Schwarz inequality and the inequality (4.12) to $\|\nabla v\|_P$ yields

$$\|\phi_b^{1/2}(b_h^P - b)\cdot\nabla v\|_P^2 \lesssim \phi_b\|b_h^P - b\|_{0,\infty,P}^2\|\nabla v\|_P^2 \lesssim |b|_{1,\infty,\Omega}h^2\|\nabla v\|_P^2 \lesssim \tau_c^{-1}\|v\|_P^2. \tag{5.16}$$

∎

Remark 5.6. Note that thanks to the assumption $b \in [W^{1,\infty}(\Omega)]^d$ and the existence of an extension operator $(\cdot)^e : W^{1,\infty}(\Omega) \to W^{1,\infty}(\mathbb{R}^d)$ (cf. section 4), a patchwise defined velocity field b_h^P satisfying Lemma 5.4, (5.12), can always be constructed, e.g., by simply taking the value of b at some point in the patch.

Next, we state and prove the main result of this section, showing that the CutDG method (3.9) for the advection-reaction problem (2.1) is inf-sup stable with respect to the $|||\cdot|||_{\mathrm{sd},h}$ norm. The main challenge here is to show that this result holds with a stability constant which is independent of the particular cut configuration.

THEOREM 5.7. *Let A_h be the bilinear form defined by* (3.9). *Then for $v \in V_h$ it holds that*

$$c_0\tau_c|||v|||_{\mathrm{sd},h} \lesssim \sup_{w\in V_h\setminus\{0\}} \frac{A_h(v,w)}{|||w|||_{\mathrm{sd},h}} \tag{5.17}$$

with the hidden constant independent of the particular cut configuration.

Proof. We follow the proof for the fitted DG method (see, for instance, [38]) to construct a suitable test function $w \in V_h$ for a given $v \in V_h$ such that (5.17) holds.

Step 1. Setting $w_1 = v$, we gain control over $|||w|||^2_{\mathrm{up},h}$, thanks to the coercivity result (5.5),

$$A_h(v,w_1) \geqslant c_0\tau_c|||v|||^2_{\mathrm{up},h}. \tag{5.18}$$

Step 2. Next, set $w_2 = \phi_b b_h^0 \cdot \nabla v$ and note that $w_2 \in V_h$ since $b_h^0 \in [\mathbb{P}_0(\mathcal{T}_h)]^d$. Then

$$\begin{aligned} A_h(v,w_2) &= \|\phi_b^{1/2} b\cdot\nabla v\|^2_\Omega + (b\cdot\nabla v, \phi_b(b_h^0 - b)\cdot\nabla v)_\Omega + (cv,w_2)_\Omega - (b\cdot nv, w_2)_{\Gamma^-} \\ &\quad - (b\cdot n[v],\{w_2\})_{\mathcal{F}_h\cap\Omega} + \frac{1}{2}(|b\cdot n|[v],[w_2])_{\mathcal{F}_h\cap\Omega} + g_h(v,w_2) \qquad (5.19)\\ &= \|\phi_b^{1/2} b\cdot\nabla v\|^2_\Omega + I + II + III + IV + V + VI. \qquad (5.20) \end{aligned}$$

Term I can be bounded by successively applying a Cauchy–Schwarz inequality and (5.13),

$$|I| \leqslant \|\phi_b^{1/2} b\cdot\nabla v\|_\Omega \|\phi_b^{1/2}(b_h^0 - b)\cdot\nabla v\|_\Omega \lesssim \|\phi_b^{1/2} b\cdot\nabla v\|_\Omega |||v|||_{\mathrm{up},h}. \tag{5.21}$$

To estimate the remaining terms II–VI, let us for the moment assume that the stability estimate

$$|||w_2|||_{\mathrm{sd},h,*} \lesssim |||v|||_{\mathrm{sd},h} \tag{5.22}$$

holds. Then one can easily see that

$$|II| + \cdots + |VI| \lesssim |||v|||_{\mathrm{up},h}|||w_2|||_{\mathrm{sd},h,*} \lesssim |||v|||_{\mathrm{up},h}|||v|||_{\mathrm{sd},h}. \tag{5.23}$$

Combining (5.21) and (5.23), we can estimate the right-hand side of (5.20) further by employing a Young inequality of the form $ab \leqslant \delta a^2 + \frac{1}{4\delta}b^2$ yielding

(5.24)

$$\begin{aligned} A_h(v,w_2) &\geqslant \|\phi_b^{1/2} b\cdot\nabla v\|^2_\Omega - \|\phi_b^{1/2} b\cdot\nabla v\|_\Omega |||v|||_{\mathrm{up},h} - C|||v|||_{\mathrm{up},h}|||v|||_{\mathrm{sd},h} \\ &\geqslant \|\phi_b^{1/2} b\cdot\nabla v\|^2_\Omega - \delta\|\phi_b^{1/2} b\cdot\nabla v\|^2_\Omega - \frac{1}{4\delta}|||v|||^2_{\mathrm{up},h} - \delta C|||v|||^2_{\mathrm{sd},h} - \frac{C}{4\delta}|||v|||^2_{\mathrm{up},h} \qquad (5.25)\\ &= (1-\delta-\delta C))\|\phi_b^{1/2} b\cdot\nabla v\|^2_\Omega - \left(\frac{1}{4\delta} + C\delta + \frac{C}{4\delta}\right)|||v|||^2_{\mathrm{up},h} \qquad (5.26)\\ &= \frac{1}{2}\|\phi_b^{1/2} b\cdot\nabla v\|^2_\Omega - \frac{(1+C)^3 + C}{2(1+C)}|||v|||^2_{\mathrm{up},h} \qquad (5.27) \end{aligned}$$

for some constant C and $\delta = \frac{1}{2+2C}$. This gives us the desired control over the streamline derivative.

Step 3. To construct a suitable test function for a given v, we set now $w_3 = w_1 + \delta c_0 \tau_c w_2$. Thanks to stability estimate (5.22) we have $|||w_3|||_{\mathrm{sd},h} \lesssim |||v|||_{\mathrm{sd},h} + \delta c_0 \tau_c |||v|||_{\mathrm{sd},h} \leqslant (1+\delta)|||v|||_{\mathrm{sd},h}$ and thus combining (5.18) and (5.27) leads us to

$$
\begin{aligned}
A_h(v, w_3) &\geqslant (1 - \delta\widetilde{C}) c_0 \tau_c |||v|||^2_{\mathrm{up},h} + \frac{\delta}{2} c_0 \tau_c \|\phi_b^{1/2} b \cdot \nabla v\|^2_\Omega \\
&\gtrsim c_0 \tau_c |||v|||^2_{\mathrm{sd},h} \gtrsim c_0 \tau_c |||v|||_{\mathrm{sd},h} |||w_3|||_{\mathrm{sd},h}
\end{aligned} \tag{5.28}
$$

for some constant $\widetilde{C}$ and $\delta > 0$ small enough. Dividing by $|||w_3|||_{\mathrm{sd},h}$ and taking the supremum over v proves (5.17). To complete the proof, it remains to establish the stability bound (5.22).

Estimate (5.22). We start by unwinding the definition of $|||\cdot|||_{\mathrm{sd},h,*}$,

$$
|||w_2|||^2_{\mathrm{sd},h,*} = \tau_c^{-1}\|w_2\|^2_\Omega + \|\phi_b^{1/2} b \cdot \nabla w_2\|^2_\Omega + \frac{1}{2}\||b\cdot n|^{1/2} w_2\|^2_\Gamma + b_c \|w_2\|^2_{\partial\mathcal{T}_h \cap \Omega} + |w_2|^2_{g_h} \tag{5.29}
$$

$$
= I + II + III + IV + V. \tag{5.30}
$$

The main tool to estimate I–V is inequality (5.14) with $P = T$, $\mathcal{P}_h = \mathcal{T}_h$, and $b_h^P = b_h^0$. Inserting the definition of $w_2 = \phi_b b_h^0 \cdot \nabla v$ and the fact that $\phi_b \tau_c^{-1} \leqslant 1$ thanks to assumption (4.8) yields

$$
I = \tau_c^{-1}\|\phi_b b_h^0 \cdot \nabla v\|^2_\Omega = \tau_c^{-1}\phi_b \|\phi_b^{1/2} b_h^0 \cdot \nabla v\|^2_\Omega \leqslant \|\phi_b^{1/2} b_h^0 \cdot \nabla v\|^2_\Omega \lesssim |||v|||^2_{\mathrm{sd},h}. \tag{5.31}
$$

The second term II can be dealt with by recalling the definition of ϕ_b, applying the inverse estimate (4.12) and subsequently moving to the streamline diffusion norm via (5.14),

$$
II = \|\phi_b^{1/2} b \cdot \nabla(\phi_b b_h^0 \cdot \nabla v)\|^2_\Omega \lesssim b_c h \|\nabla(\phi_b b_h^0 \cdot \nabla v)\|^2_\Omega \lesssim b_c h^{-1}\|\phi_b b_h^0 \cdot \nabla v\|^2_{\mathcal{T}_h} \tag{5.32}
$$

$$
\lesssim \|\phi_b^{1/2} b_h^0 \cdot \nabla v\|^2_{\mathcal{T}_h} \lesssim |||v|||^2_{\mathrm{sd},h}. \tag{5.33}
$$

Next, invoking the inverse trace estimates (4.14) followed by an application of (5.14), we see that

$$
III \lesssim b_c \|\phi_b b_h^0 \cdot \nabla v\|^2_\Gamma \lesssim \|(h\phi_b)^{1/2} b_h^0 \cdot \nabla v\|^2_\Gamma \lesssim \|\phi_b^{1/2} b_h^0 \cdot \nabla v\|^2_{\mathcal{T}_h} \lesssim |||v|||^2_{\mathrm{sd},h}, \tag{5.34}
$$

and similarly for IV,

$$
IV = b_c \|\phi_b b_h^0 \cdot \nabla v\|^2_{\partial\mathcal{T}_h \cap \Omega} \lesssim \|\phi_b^{1/2} b_h^0 \cdot \nabla v\|^2_{\mathcal{T}_h} \lesssim |||v|||^2_{\mathrm{sd},h}. \tag{5.35}
$$

After using (5.10), the remaining last term V can be estimated by proceeding as for I and II:

$$
V = |w_2|^2_{g_c} + |w_2|^2_{g_b} \lesssim \tau_c^{-1}\|w_2\|^2_{\mathcal{T}_h} + \|\phi_b^{1/2} b_h^0 \cdot \nabla w_2\|^2_{\mathcal{T}_h} \lesssim |||v|||^2_{\mathrm{sd},h}. \tag{5.36}
$$
$\square$

We conclude this section with a couple of remarks, elucidating the role of the ghost penalties g_c and g_b.

Remark 5.8. We point out that the most critical part in the derivation of the inf-sup condition (5.17) is the proof of the stability estimate (5.22). At several occasions it involves inverse estimates of the form (4.12)–(4.14) to pass from $w_2 = \phi_b b_h^0 \cdot \nabla v$ to v in the streamline diffusion norm. As a result, we need to control the streamline derivative of v on the *entire* active mesh $\mathcal{T}_h$, which is precisely the role of the ghost penalty g_b.

Remark 5.9. The role of the ghost penalty g_c is twofold. In the previous proof, the ghost penalty g_c is only needed to pass between b and b_h^0 by controlling various norm expressions involving $b - b_h^0$ and v in terms of $\tau_c^{-1/2}\|v\|_{\mathcal{T}_h}$. Consequently, the ghost penalty g_c could have been omitted if $b \in [\mathbb{P}_1(\mathcal{T}_h)]^d$ since then $\phi_b b \cdot \nabla v \in V_h$. Nevertheless, we will see that g_c is indeed needed to ensure that the condition number of the system matrix is robust with respect to the boundary position relative to the background mesh; see section 7.

Remark 5.10. The previous derivation raises the question of whether the ghost penalty g_b is needed only because of the use of the stronger norm $|||\cdot|||_{\mathrm{sd}}$ instead of the more classical $|||\cdot|||_{\mathrm{up}}$ norm. A closer look at the numerical analysis based on the $|||\cdot|||_{\mathrm{up}}$ norm as presented in [13] reveals that g_b cannot be avoided when $\mathbb{P}_k$ elements with $k \geqslant 1$ are used. The reason is that the a priori analysis based on $|||\cdot|||_{\mathrm{up}}$ exploits the orthogonality of the L^2 projection operator π_h to rewrite the advection related term in (5.1) to

$$(\pi_h u - u, b \cdot \nabla v)_\Omega = (\pi_h u - u, (b - b_h^0) \cdot \nabla v)_\Omega \tag{5.37}$$

to arrive at an optimal error estimate for the advection related error terms in the $|||u - u_h|||_{\mathrm{up}}$ norm. In the unfitted case though, it is not possible to define a *stable* orthogonal projection operator using the L^2 scalar product $(\cdot,\cdot)_\Omega$ considering only the physical domain Ω. The orthogonality of the unfitted L^2 projection π_h^e constructed in section 4 is perturbed as it satisfies only $(\pi_h^e u - u^e, v)_{\mathcal{T}_h} = 0$ for $v \in V_h$. Therefore, we get now

$$(\pi_h^e u - u^e, b \cdot \nabla v)_\Omega = (\pi_h^e u - u^e, (b - b_h^0) \cdot \nabla v)_\Omega + (\pi_h u^e - u^e, b_h^0 \cdot \nabla v)_{\mathcal{T}_h \setminus \Omega}, \tag{5.38}$$

and thus we need to provide sufficient control of $\|\phi_b^{1/2} b_h^0 \cdot \nabla v\|_{\mathcal{T}_h \setminus \Omega}$ in the relevant norms to handle the second term in (5.38) for $k \geqslant 1$. For $v \in \mathbb{P}_0$ on the other hand, (5.38) vanishes, and thus no additional advection related CutDG stabilizations are needed.

6. A priori error analysis.

We turn to the a priori error analysis of the unfitted discretization scheme (3.9). To keep the technical details at a moderate level, we assume for a priori error analysis that the contributions from the cut elements $\mathcal{T}_h \cap \Omega$, the cut faces $\mathcal{F}_h \cap \Omega$, and the boundary parts $\Gamma \cap \mathcal{T}_h$ can be computed exactly. For a thorough treatment of variational crimes arising from the discretization of a curved boundary, we refer the reader to [78, 24, 54]. We start with quantifying the effect of the stabilization g_h on the consistency of the total bilinear form A_h defined by (3.9).

LEMMA 6.1 (weak Galerkin orthogonality). *Let $u \in H^1(\Omega)$ be the solution*[1] *to* (2.1) *and let u_h be the solution to the discrete formulation* (3.9). *Then*

$$a_h(u - u_h, v) - g_h(u_h, v) = 0. \tag{6.1}$$

Proof. The proof is a direct consequence of the fact that u satisfies $a_h(u, v) = l_h(v)\ \forall\, v \in V_h$. □

THEOREM 6.2 (a priori error estimate for $p \geqslant 1$). *For $s \geqslant 2$, let $u \in H^s(\Omega)$ be the solution to the advection-reaction problem* (2.1) *and let u_h be the solution to the*

[1] We assume $u \in H^1(\Omega)$ to simplify the presentation, but weaker regularity assumptions can be made; see, for instance, [38].

stabilized CutDG formulation (3.9)*. Then with* $r = \min\{s, p+1\}$ *with* $p \geqslant 1$ *it holds that*

$$|||u - u_h|||_{\mathrm{sd}} \lesssim (c_0\tau_c)^{-1} b_c^{1/2} h^{r-1/2} \|u\|_{r,\Omega}. \tag{6.2}$$

Proof. Decompose $u - u_h$ into a projection error $e_\pi = u - \pi_h u$ and a discrete error $e_h = \pi_h u - u_h$. Thanks to the interpolation estimate (4.24), it is enough to estimate the discrete error e_h for which the inf-sup condition (5.17) implies that

$$c_0\tau_c |||e_h|||_{\mathrm{sd},h} \lesssim \sup_{v \in V_h \setminus \{0\}} \frac{A_h(e_h, v)}{|||v|||_{\mathrm{sd},h}} \tag{6.3}$$

$$= \sup_{v \in V_h \setminus \{0\}} \frac{a_h(e_\pi, v) + g_h(\pi_h u, v)}{|||v|||_{\mathrm{sd},h}} \tag{6.4}$$

$$\lesssim \sup_{v \in V_h \setminus \{0\}} \frac{|||e_\pi|||_{\mathrm{sd},*} |||v|||_{\mathrm{sd}} + |\pi_h u|_{g_h} |v|_{g_h}}{|||v|||_{\mathrm{sd},h}} \tag{6.5}$$

$$\lesssim |||e_\pi|||_{\mathrm{sd},*} + |\pi_h u|_{g_h}. \tag{6.6}$$

Recalling assumption (4.8) and its reformulation (4.9), the bounds for the consistency and approximation error stated in Assumption HP1 and (4.24) show that

$$|||u - u_h|||_{\mathrm{sd}} \lesssim |||e_\pi|||_{\mathrm{sd}} + |||e_h|||_{\mathrm{sd},h} \lesssim (c_0\tau_c)^{-1}(|||e_\pi|||_{\mathrm{sd},*} + |\pi_h u|_{g_h}) \tag{6.7}$$

$$\lesssim (c_0\tau_c)^{-1}(\tau_c^{1/2} h^{1/2} + b_c^{1/2}) h^{r-1/2} \|u\|_{r,\Omega} \lesssim (c_0\tau_c)^{-1} b_c^{1/2} h^{r-1/2} \|u\|_{r,\Omega}, \tag{6.8}$$

which concludes the proof. ∎

We conclude this section by considering the particular case of $\mathbb{P}_0$ elements. First observe that since $b \cdot \nabla v = 0$ for $v \in \mathbb{P}_0(\mathcal{T}_h)$, all terms in (5.38) vanish. Referring to Remark 5.10, we therefore do not need the $|||\cdot|||_{\mathrm{sd},h}$ norm to control the remainder term in (5.38). Instead, we can work in the weaker and unstabilized $|||\cdot|||_{\mathrm{up}}$ norm to derive an optimal a priori error estimate.

Proposition 6.3 (a priori error estimate for $p = 0$). *For* $s \geqslant 1$*, let* $u \in H^s(\Omega)$ *be the solution to the advection-reaction problem* (2.1) *and let* u_h *be the solution to the* unstabilized *CutDG formulation* (3.9) *with* $g_h = 0$*. Then,*

$$|||u - u_h|||_{\mathrm{up}} \lesssim (c_0\tau_c)^{-1} b_c^{1/2} h^{1/2} \|u\|_{1,\Omega}. \tag{6.9}$$

Proof. The proof follows verbatim the standard arguments; see, e.g., [13, 38]. Starting from the discrete error $e_h = \pi_h u - u_h$, Remark 5.2 together with the representation (5.1) and the fact that $b \cdot \nabla e_h = 0$ implies that

$$c_0\tau_c |||e_h|||_{\mathrm{up}}^2 \lesssim a_h(e_h, e_h) \tag{6.10}$$

$$= a_h(e_\pi, e_h) \tag{6.11}$$

$$= ((c - \nabla \cdot b)e_\pi, e_h)_{\mathcal{T}_h \cap \Omega} + (b \cdot n e_\pi, e_h)_{\Gamma^+}$$

$$+ (b \cdot n\{e_\pi\}, [e_h])_{\mathcal{F}_h \cap \Omega} + \frac{1}{2}(|b \cdot n|[e_\pi], [e_h])_{\mathcal{F}_h \cap \Omega} \tag{6.12}$$

$$\lesssim |||e_\pi|||_{\mathrm{up},*} |||e_h|||_{\mathrm{up}}, \tag{6.13}$$

where we defined the auxiliary norm $|||v|||_{\mathrm{up},*}$ by $|||v|||_{\mathrm{up},*}^2 = |||v|||_{\mathrm{up}}^2 + b_c\|v\|_{\partial\mathcal{T}_h \cap \Omega}^2$. Now the result follows from (4.24) since $|||e_\pi|||_{\mathrm{up},*} \leqslant |||e_\pi|||_{\mathrm{sd},h,*}$. ∎

Remark 6.4. The previous proposition shows that geometrically robust optimal a priori error estimates can be obtained for an unfitted $\mathbb{P}_0$ based discretization of the *stationary* advection-reaction problem, *even without employing any ghost penalties*. Nevertheless, without adding g_c, the resulting system matrix will be severely ill-conditioned in the presence of small cut elements; see section 7. Similarly, an explicit time-stepping method for the time-dependent advection-reaction problem will suffer from severe time-step restrictions if the mass matrix is not sufficiently stabilized, which motivates the introduction of the stabilized L^2 scalar product in (3.14).

7. Condition number estimates. We now conclude the numerical analysis of the CutDG method for the advection-reaction problem by showing that the condition number associated with the bilinear form (3.9) can be bounded by Ch^{-1} with a constant independent of particular cut configuration. Our derivation is inspired by the presentation in [41].

Let $\{\phi_i\}_{i=1}^N$ be the standard piecewise polynomial basis functions associated with $V_h = \mathbb{P}_p(\mathcal{T}_h)$ so that any $v \in V_h$ can be written as $v = \sum_{i=1}^N V_i \phi_i$ with coefficients $V = \{V_i\}_{i=1}^N \in \mathbb{R}^N$. The system matrix $\mathcal{A}$ associated with A_h is defined by the relation

$$(\mathcal{A}V, W)_{\mathbb{R}^N} = A_h(v,w) \quad \forall\, v, w \in V_h. \tag{7.1}$$

Thanks to the L^2 coercivity of A_h, the system matrix $\mathcal{A}$ is a bijective linear mapping $\mathcal{A} : \mathbb{R}^N \to \mathbb{R}^N$ with its operator norm and condition number defined by

$$\|\mathcal{A}\|_{\mathbb{R}^N} = \sup_{V \in \mathbb{R}^N \setminus \{0\}} \frac{\|\mathcal{A}V\|_{\mathbb{R}^N}}{\|V\|_{\mathbb{R}^N}} \quad \text{and} \quad \kappa(\mathcal{A}) = \|\mathcal{A}\|_{\mathbb{R}^N} \|\mathcal{A}^{-1}\|_{\mathbb{R}^N}, \tag{7.2}$$

respectively. To pass between the discrete l^2 norm of coefficient vectors V and the continuous L^2 norm of finite element functions v_h, we need to recall the well-known estimate

$$h^{d/2} \|V\|_{\mathbb{R}^N} \lesssim \|v\|_{L^2(\mathcal{T}_h)} \lesssim h^{d/2} \|V\|_{\mathbb{R}^N}, \tag{7.3}$$

which holds for any quasi-uniform mesh $\mathcal{T}_h$ and $v \in V_h$. Then we can prove the following theorem.

THEOREM 7.1. *The condition number of the system matrix $\mathcal{A}$ associated with* (3.9) *satisfies*

$$\kappa(\mathcal{A}) \lesssim b_c (c_0 h)^{-1} \tag{7.4}$$

independently of how the boundary Γ cuts the background mesh $\mathcal{T}_h$.

Proof. The definition of the condition number requires bounding $\|\mathcal{A}\|_{\mathbb{R}^N}$ and $\|\mathcal{A}^{-1}\|_{\mathbb{R}^N}$.

Estimate of $\|\boldsymbol{\mathcal{A}}\|_{\mathbb{R}^N}$. We start by estimating $A_h(v,w) = a_h(v,w) + g_h(v,w)\ \forall\, v, w \in V_h$. To bound the first term a_h, successively employ a Cauchy–Schwarz inequality and the inverse trace inequalities (4.13) and (4.14) to obtain

$$a_h(v,w) \lesssim \|c\|_{0,\infty,\Omega} \|v\|_\Omega \|w\|_\Omega + \|b \cdot \nabla v\|_\Omega \|w\|_\Omega + \||b \cdot n|^{1/2} v\|_\Gamma \||b \cdot n|^{1/2} w\|_\Gamma \tag{7.5}$$

$$\qquad + \||b \cdot n|^{1/2} v\|_{\mathcal{F}_h \cap \Omega} \||b \cdot n|^{1/2} w\|_{\mathcal{F}_h \cap \Omega} \tag{7.6}$$

$$\qquad \lesssim \|c\|_{0,\infty,\Omega} \|v\|_\Omega \|w\|_\Omega + h^{-1} b_c \|v\|_{\mathcal{T}_h} \|w\|_{\mathcal{T}_h} \lesssim h^{-1} b_c \|v\|_{\mathcal{T}_h} \|w\|_{\mathcal{T}_h}, \tag{7.7}$$

where we used (4.9) in the last step. Next, note that by assumption (5.10), we have that

$$|v|_{g_h}^2 \lesssim \|b \cdot \nabla v\|_{\mathcal{T}_h}^2 + \tau_c^{-1}\|v\|_{\mathcal{T}_h}^2 \lesssim b_c h^{-1}\|v\|_{\mathcal{T}_h}^2, \tag{7.8}$$

and thus

$$g_h(v,w) \lesssim |v|_{g_h}|w|_{g_h} \lesssim b_c h^{-1}\|v\|_{\mathcal{T}_h}\|w\|_{\mathcal{T}_h}. \tag{7.9}$$

As a result of these estimates and (7.3), we have

$$A_h(v,w) \lesssim b_c h^{-1}\|v\|_{\mathcal{T}_h}\|w\|_{\mathcal{T}_h} \lesssim b_c h^{d-1}\|V\|_{\mathbb{R}^N}\|W\|_{\mathbb{R}^N}, \tag{7.10}$$

which allows us to estimate $\|\mathcal{A}\|_{\mathbb{R}^N}$ by

$$\|\mathcal{A}\|_{\mathbb{R}^N} = \sup_{V\in\mathbb{R}^N\setminus\{0\}}\ \sup_{W\in\mathbb{R}^N\setminus\{0\}} \frac{(\mathcal{A}V,W)_{\mathbb{R}^N}}{\|V\|_{\mathbb{R}^N}\|W\|_{\mathbb{R}^N}} \tag{7.11}$$

$$= \sup_{V\in\mathbb{R}^N\setminus\{0\}}\ \sup_{W\in\mathbb{R}^N\setminus\{0\}} \frac{A_h(v,w)}{\|V\|_{\mathbb{R}^N}\|W\|_{\mathbb{R}^N}} \lesssim b_c h^{d-1}. \tag{7.12}$$

Estimate of $\|\boldsymbol{\mathcal{A}}^{-1}\|_{\mathbb{R}^N}$. The discrete coercivity result (5.5) and assumption (5.9) imply that

$$A_h(v,v) \gtrsim c_0\tau_c |||v|||_{\mathrm{up},h}^2 \gtrsim c_0\|v\|_{\mathcal{T}_h}^2 \gtrsim c_0 h^d\|V\|_{\mathbb{R}^N}^2, \tag{7.13}$$

and as a result,

$$\|\mathcal{A}V\|_{\mathbb{R}^N} = \sup_{W\in\mathbb{R}^N\setminus\{0\}} \frac{(\mathcal{A}V,W)_{\mathbb{R}^N}}{\|W\|_{\mathbb{R}^N}} \geqslant \frac{(\mathcal{A}V,V)_{\mathbb{R}^N}}{\|V\|_{\mathbb{R}^N}} = \frac{A_h(v,v)}{\|V\|_{\mathbb{R}^N}} \gtrsim c_0 h^d\|V\|_{\mathbb{R}^N}. \tag{7.14}$$

Setting $V = \mathcal{A}^{-1}W$, the previous chain of estimates shows that $\|\mathcal{A}^{-1}\|_{\mathbb{R}^n} \lesssim c_0^{-1}h^{-d}$, which in combination with (7.12) gives the desired bound

$$\|\mathcal{A}\|_{\mathbb{R}^N}\|\mathcal{A}^{-1}\|_{\mathbb{R}^N} \lesssim b_c(c_0 h)^{-1}. \tag{7.15}$$

□

8. Ghost penalty realizations.

In this section, we present a number of possible realizations of the ghost penalty operators satisfying our Assumptions HP1, HP2, and HP3. We briefly discuss the L^2 norm related ghost penalty g_c first and then derive corresponding realizations of g_b. So far, three construction principles exist in the literature. The first one is the classical *face-based* ghost penalty proposed by [7] for continuous $\mathbb{P}_1$ elements. High-order variants were then introduced in [15]; for a detailed analysis we refer to [15, 83]. In face-based ghost penalties, jumps of normal derivatives of all relevant polynomial orders across faces belonging to the face set

$$\mathcal{F}_h^g = \{F \in \mathcal{F}_h : T^+ \cap \Gamma \neq \emptyset \vee T^- \cap \Gamma \neq \emptyset\} \tag{8.1}$$

are penalized. For our current problem class, the corresponding DG variant extending the L^2 norm is given by

$$g_c^f(v,w) = \gamma_c^f c_0 \sum_{j=0}^{p} h^{2j+1}([\partial_n^j v],[\partial_n^j w])_{\mathcal{F}_h^g}, \tag{8.2}$$

where the notation $\partial_n^j v \coloneqq \sum_{|\alpha|=j} \frac{D^\alpha v(x) n^\alpha}{\alpha!}$ for multi-indices $\alpha = (\alpha_1, \dots, \alpha_d)$, $|\alpha| = \sum_i \alpha_i$, and $n^\alpha = n_1^{\alpha_1} n_2^{\alpha_2} \cdots n_d^{\alpha_d}$ is used. The constant γ_c^f denotes a dimensionless stability parameter.

In [15] and later in [22], alternative ghost penalties were proposed which were based on a *local projection stabilization*. For a given patch P of $\operatorname{diam}(P) \lesssim h$ containing the two elements T_1 and T_2, one defines the L^2 projection $\pi_P : L^2(P) \to \mathbb{P}_p(P)$ onto the space of polynomials of order p associated with the patch P. For $v \in V_h$, the fluctuation operator $\kappa_P = \operatorname{Id} - \pi_P$ measures then the deviation of $v|_P$ from being a polynomial defined on P. By choosing certain patch definitions, a coupling between elements with a possible small cut and those with a fat intersection is ensured. One patch choice arises naturally from the definition of $\mathcal{F}_h^g$ by defining the patch $P(F) = T_F^+ \cup T_F^-$ for two elements T_F^+, T_F^- sharing the interior face F and setting

$$\mathcal{P}_1 = \{P(F)\}_{F \in \mathcal{F}_h^g}. \tag{8.3}$$

A second possibility is to use neighborhood patches $\omega(T)$,

$$\mathcal{P}_2 = \{\omega(T)\}_{T \in \mathcal{T}_\Gamma}. \tag{8.4}$$

Finally, one can mimic the cell agglomeration approach taken in classical unfitted DG approaches [5, 65, 103, 70] by associating to each cut element $T \in \mathcal{T}_\Gamma$ with a small intersection $|T \cap \Omega|_d \ll |T|_d$ an element $T' \in \omega(T)$ satisfying the fat intersection property $|T' \cap \Omega|_d \geqslant c_s |T'|^d$. Introducing the "agglomerated patch" $P_a(T) = T \cup T'$, a proper collection of patches is given by

$$\mathcal{P}_3 = \{P_a(T) \mid T \in \mathcal{T}_\Gamma \wedge |T \cap \Omega|_d \leqslant c_s |T|_d\}. \tag{8.5}$$

The resulting *local projection* based ghost penalty extending the L^2 norm in the sense of HP2 is then defined as follows:

$$g_c^p(v, w) = \gamma_c^p c_0 \sum_{P \in \mathcal{P}} (\kappa_P v, \kappa_P w)_P, \quad \mathcal{P} \in \{\mathcal{P}_1, \mathcal{P}_2, \mathcal{P}_3\}. \tag{8.6}$$

Finally, an elegant version of a patch-based ghost penalty avoiding the assembly of local projection matrices completely was recently proposed in [92]. Using the natural global polynomial extension u_i^e every polynomial u_i on an element T_i possesses, a volume based jump on a patch $P = T_1 \cup T_2$ can be defined by $[u]_P = u_1^e - u_2^e$ which gives rise to the *volume based* ghost penalty

$$g_c^v(v, w) = \gamma_b^v c_0 \sum_{P \in \mathcal{P}} ([v]_P, [w]_P)_P, \quad \mathcal{P} \in \{\mathcal{P}_1, \mathcal{P}_3\}. \tag{8.7}$$

LEMMA 8.1. *Each of the face, projection, and volume based realizations of g_c satisfies Assumptions* HP1 *and* HP2.

Proof. As the original proofs require only minimal adaption to derive HP1 and HP2 for discontinuous ansatz functions instead of continuous ones, we refer to [15] and [83] for the analysis of g_h^p and g_h^f and to [92] for the volume penalty g_h^v. ∎

Next, we design proper realizations of the advection related ghost penalty g_b. The natural idea is to start from g_c and to replace v with $\phi_b^{1/2} b \cdot \nabla v$ as we wish to control the L^2 norm of the scaled streamline derivative. This idea leads us to the following lemma.

LEMMA 8.2. *Each of the face, projection, and volume based realizations of g_b defined by*

$$g_b^f(v,w) = \gamma_b^f \sum_{j=0}^{p} \phi_b h^{2j+1} \left([b_h^P \cdot \nabla \partial_n^j v], [b_h^P \cdot \nabla \partial_n^j w]\right)_{\mathcal{F}_h^g}, \tag{8.8}$$

$$g_b^p(v,w) = \gamma_b^p \sum_{P\in\mathcal{P}} \phi_b \left(\kappa_p \left(b_h^P \cdot \nabla v\right), \kappa_p \left(b_h^P \cdot \nabla w\right)\right)_P, \quad \mathcal{P} \in \{\mathcal{P}_1, \mathcal{P}_2, \mathcal{P}_3\}, \tag{8.9}$$

$$g_b^v(v,w) = \gamma_b^v \sum_{P\in\mathcal{P}} \phi_b \left([b_h^P \cdot \nabla v]_P, [b_h^P \cdot \nabla w]_P\right)_P, \quad \mathcal{P} \in \{\mathcal{P}_1, \mathcal{P}_3\}, \tag{8.10}$$

satisfies Assumption HP1 *and* HP3. *Here, we choose b_h^P to be a patchwise defined, constant vector-valued function satisfying the assumptions of Lemma* 5.4. *For g_b^f, the vector field b_h^P is understood to be defined on each face patch $P(F) = T_F^+ \cup T_F^-$.*

Proof. Here, we consider only g_b^v as the analysis for g_b^p and g_b^f is rather similar, and a detailed theoretical analysis of the g_b^f can also be found in [86].

We start with the verification of Assumption HP3. First recall that for two adjacent elements T_1 and T_2 and $P = T_1 \cup T_2$, the norm equivalence $\|w\|_{T_1}^2 \sim \|w\|_{T_2}^2 + \|[w]_P\|_P^2$ holds for $w \in V_h$. Setting $w = \phi_b^{1/2} b_h^P \cdot \nabla v$ and using Lemma 5.4, (5.13), to pass between $\phi_b^{1/2} b_h^P \cdot \nabla v$ and $\phi_b^{1/2} b.\nabla v$, we conclude that

$$\|\phi_b^{1/2} b \cdot \nabla v\|_{T_1}^2 \lesssim \|\phi_b^{1/2} b_h^P \cdot \nabla v\|_{T_1}^2 + \|\phi_b^{1/2}(b_h^P - b)\cdot \nabla v\|_{T_1}^2 \tag{8.11}$$

$$\lesssim \|\phi_b^{1/2} b_h^P \cdot \nabla v\|_{T_1}^2 + \tau_c^{-1}\|v\|_{T_1}^2 \tag{8.12}$$

$$\lesssim \|\phi_b^{1/2} b_h^P \cdot \nabla v\|_{T_2}^2 + \|[\phi_b^{1/2} b_h^P \cdot \nabla v]_P\|_P^2 + \tau_c^{-1}\|v\|_{T_1}^2 \tag{8.13}$$

$$\lesssim \|\phi_b^{1/2} b \cdot \nabla v\|_{T_2}^2 + \tau_c^{-1}\|v\|_{T_2}^2 + \|[\phi_b^{1/2} b_h^P \cdot \nabla v]_P\|_P^2 + \tau_c^{-1}\|v\|_{T_1}^2. \tag{8.14}$$

This together with the geometric Assumption G2 and the norm equivalence $\|\phi_b^{1/2} b\cdot\nabla v\|_{T_2}^2 \sim \|\phi_b^{1/2} b\cdot\nabla v\|_{T_2\cap\Omega}^2$ on elements T_2 with a fat intersection implies that

$$\|\phi_b^{1/2} b\cdot\nabla v\|_{\mathcal{T}_h}^2 \lesssim \|\phi_b^{1/2} b\cdot\nabla v\|_{\Omega}^2 + |v|_{g_b^v}^2 + \tau_c^{-1}\|v\|_\Omega^2 + |v|_{g_c}^2, \tag{8.15}$$

proving the first inequality in Assumption HP3. The second inequality easily follows from Assumption HP3, implying that $|v|_{g_c}^2 \lesssim \tau_c^{-1}\|v\|_{\mathcal{T}_h}^2$ and the fact that $|v|_{g_b^v}^2 \lesssim \|\phi_b^{1/2} b\cdot\nabla v\|_{\mathcal{P}}^2 + \tau_c^{-1}\|v\|_{\mathcal{P}}^2$.

To prove the weak consistency Assumption HP1, simply observe that $[\phi_b^{1/2} b_h^P \cdot \nabla \pi_p u^e]_P = 0$ for $u \in H^s(\Omega)$, $s \geqslant 1$, and the patchwise defined L^2 projection π_P, and thus

$$\sum_{P\in\mathcal{P}} \|[\phi_b^{1/2} b_h^P \cdot \nabla \pi_h^e u]\|_P^2 = \sum_{P\in\mathcal{P}} \|[\phi_b^{1/2} b_h^P \cdot \nabla\left(\pi_h^e u - \pi_P u^e\right)]\|_P^2 \tag{8.16}$$

$$\lesssim \sum_{P\in\mathcal{P}} \|\phi_b^{1/2} b_h^P \cdot \nabla\left(\pi_h^e u - u^e\right)\|_P^2 + \sum_{P\in\mathcal{P}} \|\phi_b^{1/2} b_h^P \cdot \nabla\left(u - \pi_P u^e\right)\|_P^2 \tag{8.17}$$

$$\lesssim \phi_b b_c^2 h^{2(r-1)} \|u^e\|_{r,\mathcal{T}_h}^2 \lesssim b_c h^{2r-1}\|u\|_{r,\Omega}^2, \tag{8.18}$$

which concludes the proof. ∎

Remark 8.3. It is possible to replace the convection and reaction related stabilization forms g_b and g_c by a unified ghost penalty. For instance, for the face-based realizations (8.2) and (8.8), a single ghost penalty of the form

$$g^f(v,w) = \gamma^f \sum_{j=0}^{p} \Big(c_0 + \frac{b_c}{h}\Big) h^{2j+1} \left([\partial_n^j v], [\partial_n^j w]\right)_{\mathcal{F}_h^g} \tag{8.19}$$

can be used instead, at the cost of introducing some additional (order-preserving) crosswind diffusion. Consequently, only face jump penalties of the form $[\partial_n^j(\cdot)]$ need to be implemented. We refer to [86, Remark 3.4] for a detailed discussion.

9. Time-stepping. After the detailed theoretical analysis of the stabilized CutDG method for the stationary advection-reaction problem in the previous sections, we now formulate a CutDG method for the time-dependent problem (3.13). The presented formulation is only a first demonstration of how ghost penalty techniques can be employed to devise explicit time-stepping methods which do not suffer from a severe time-step restriction caused by small cut elements. A detailed theoretical analysis is beyond the scope of the present work and will be the subject of a forthcoming paper.

Following and extending the notation in section 10.1.2, the mass matrix $\mathcal{M}$ associated with the stabilized L^2 inner product is defined by the relation

$$(\mathcal{M}V, W)_{\mathbb{R}^N} = M_h(v,w) \quad \forall\, v,w \in V_h, \tag{9.1}$$

where again $V, W \in \mathbb{R}^N$ denote the coefficient vectors of v and w. Denoting the time-dependent coefficient vector $U(t) \in \mathbb{R}^N$ associated with the semidiscrete solution $u_h(t)$, we are left with solving a system of the form

$$U'(t) = \mathcal{L}U(t) + F(t), \tag{9.2a}$$

$$U(0) = U_0, \tag{9.2b}$$

where we set $\mathcal{L} = \mathcal{M}^{-1}\mathcal{A}$ and define the vector $F(t) \in \mathbb{R}^N$ by the relation $(\mathcal{M}V, F(t))_{\mathbb{R}^N} = (f(t), v_h)_\Omega$; that is, F is the usual load vector premultiplied with $\mathcal{M}^{-1}$. To arrive at a fully discrete system, we shall use either the forward Euler method,

$$U^{n+1} = U^n + \Delta t \left(\mathcal{L}U^n + F(t^n)\right), \tag{9.3}$$

or the following explicit third-order Runge–Kutta method taken from [38, 18]:

(9.4a)

$$U^{n,1} = U^n + \Delta t(\mathcal{L}U^n + F(t^n)),$$

(9.4b)

$$U^{n,2} = \frac{1}{2}(U^n + U^{n,1}) + \frac{\Delta t}{2}(\mathcal{L}U^n + F(t^n) + \Delta t F'(t^n)),$$

(9.4c)

$$U^{n+1} = \frac{1}{3}(U^n + U^{n,1} + U^{n,2}) + \frac{\Delta t}{3}\left(\mathcal{L}U^{n,2} + F(t^n) + \Delta t F'(t^n) + \frac{\Delta t^2}{2}F''(t^n)\right).$$

In (9.4), $U^{n,s}$, $s \in \{1,2\}$, denote the intermediate stages. For simplicial meshes, the combination of these time-stepping methods with the standard fitted DG method that corresponds to (3.13) was studied in [18, 38]. It was shown that under a hyperbolic CFL condition: $\Delta t = Ch$, (9.3) combined with $\mathbb{P}_0(\mathcal{T}_h)$ converges as $\mathcal{O}(h^{1/2}+\Delta t)$, and (9.4) combined with $\mathbb{P}_2(\mathcal{T}_h)$ converges as $\mathcal{O}(h^{5/2}+\Delta t^3)$. For details, we refer to [38, section 3.1] and [18].

Remark 9.1. If the mass matrix related ghost penalty g_m uses face-based stabilizations of the form (8.2) together with the face set (8.1), the mass matrix will no longer be block diagonal as in standard noncut DG methods, since the elements in $\mathcal{T}_\Gamma$ are interlaced with each other through the face set $\mathcal{F}_h^g$. As a remedy, one could employ local projection or volume based ghost penalties instead, together with a more careful choice of the associated patches $\mathcal{P}$, so that in the vicinity of the embedded boundary, the mass matrix can be inverted locally on patches.

10. Numerical results. This section is devoted to a number of numerical experiments supporting our theoretical findings. We first investigate the method (3.9) for the stationary problem. Convergence rate studies for smooth manufactured solutions defined on complex 2D and 3D domains are presented to demonstrate the applicability of our method to nontrivial domain geometries. The goal of the second, more detailed convergence study is twofold. First, we examine the experimental order of convergence (EOC) when using higher-order elements up to degree $p = 3$. Second, using the same domain setup, we consider a typical test case of a rough solution with a sharp internal layer to illustrate that the proposed CutDG method possesses the same robustness as the corresponding standard fitted DG method. We then consider two numerical studies illustrating the importance of the ghost penalties for the geometrical robustness of the derived a priori error and condition number estimates. Finally, we conclude this section with a brief study of the time-dependent method (3.13). As for the stationary problem, we examine both the order of convergence and the geometrical robustness of the method.

10.1. Convergence rate experiments. In the first series of experiments, we test the convergence of the proposed stationary CutDG method (3.9) over various geometries, dimensions, and polynomial orders. Common to all examples below, a background mesh $\widetilde{\mathcal{T}}_0$ for the embedding domain $\widetilde{\Omega} = [-a, a]^d$ is generated and successively refined, from which the active background meshes $\{\mathcal{T}_k\}_{k=0}^N$ are extracted. The mesh size is then given by $h_k = 2a \cdot 2^{-3-k}$. For a given polynomial order p and active mesh $\mathcal{T}_k$, we compute the numerical solution $u_k^p \in \mathbb{P}_p(\mathcal{T}_k)$ from (3.9) using the ghost penalties defined in (8.8) and (8.2). The EOC shown in the convergence tables below is calculated using

$$\mathrm{EOC}(k, p) = \frac{\log(E_{k-1}^p / E_k^p)}{\log(h_{k-1}/h_k)}, \tag{10.1}$$

where $E_k^p = \|e_k^p\| = \|u - u_k^p\|$ denotes the error of the numerical approximation u_k^p measured in a certain (semi-)norm $\|\cdot\|$. The error norms considered in our tests are the L^2 norm $\|\cdot\|_\Omega$, the upwind flux seminorm $\frac{1}{\sqrt{2}}\||b\cdot n|^{1/2}[\cdot]\|_{\mathcal{F}_h}$, the streamline diffusion seminorm $\|\phi^{1/2} b \cdot \nabla(\cdot)\|_\Omega$, as well as the weighted L^2 norm $\frac{1}{\sqrt{2}}\||b\cdot n|^{1/2}(\cdot)\|_\Gamma$, in accordance with the a priori error estimate presented in section 6. In addition, we also tabulate EOCs for the $\|\cdot\|_\Gamma$ and $\|\cdot\|_{L^\infty(\Omega)}$ norms.

10.1.1. Flower and popcorn domains. To demonstrate the capability of the presented CutDG method to treat complex geometries in different dimensions, we consider two test cases. In the first test case, the advection-reaction problem (2.1) is numerically solved over a 2D flower domain that is defined by

$$\Omega = \{(x, y) \in \mathbb{R}^2 \mid \phi(x, y) < 0\} \quad \text{with } \Phi(x, y) = \sqrt{x^2 + y^2} - r_0 - r_1 \cos(5 \operatorname{atan}_2(y, x)) \tag{10.2}$$

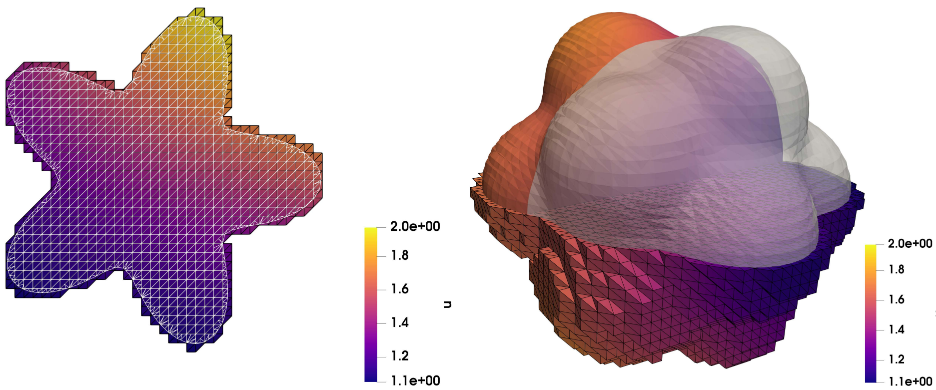

FIG. 10.1. *Solution plots for* 2D *flower (left) and* 3D *popcorn (right) examples. In both cases the solution is plotted over the active background mesh and domain boundaries, and physical domains are shown as well.*

with $r_0 = 0.5$ and $r_1 = 0.15$; see Figure 10.1 (left). The manufactured solution u, the velocity field b, and the reaction term c are taken from [68] and given by

$$u(x,y) = 1 + \sin(\pi(1+x)(1+y)^2/8), \quad b(x,y) = (0.8, 0.6), \quad c = 1.0. \tag{10.3}$$

For the 3D test case, the domain of interest is a popcorn-like geometry defined by

(10.4)
$$\Phi(x,y,z) = \sqrt{x^2+y^2+z^2} - r_0 - \sum_{k=0}^{11} A \exp\left(-((x-x_k)^2 + (y-y_k)^2 + (z-z_k)^2)/\sigma^2\right),$$

where

$$\begin{aligned}
(x_k, y_k, z_k) &= \frac{r_0}{\sqrt{5}}\left(2\cos\left(\frac{2k\pi}{5}\right), 2\sin\left(\frac{2k\pi}{5}\right), 1\right), \quad 0 \le k \le 4,\\
(x_k, y_k, z_k) &= \frac{r_0}{\sqrt{5}}\left(2\cos\left(\frac{(2(k-5)-1)\pi}{5}\right), 2\sin\left(\frac{(2(k-5)-1)\pi}{5}\right), -1\right), \quad 5 \le k \le 9,\\
(x_k, y_k, z_k) &= (0, 0, r_0), \quad k = 10,\\
(x_k, y_k, z_k) &= (0, 0, -r_0), \quad k = 11,
\end{aligned}$$

and

$$r_0 = 0.6, \sigma = 0.2, A = 2;$$

see Figure 10.1 (right). This time, we set the manufactured solution u, the vector field b, and the reaction term c to

(10.5)
$$u(x,y,z) = 1 + \sin(\pi(1+x)(1+y^2)(1+z^3)/8), \quad b(x,y,z) = (0.8, 0.6, 0.4), \quad c = 1.0.$$

For both examples we employ linear elements together with stabilization parameters $\gamma_b^f = \gamma_c^f = 0.01$. The calculated EOCs are summarized in Table 10.1 and confirm the theoretically expected convergence rates of $\mathcal{O}(h^{3/2})$. For the L^2 norm, we even observe second-order convergence for these particular examples and mesh definitions, but we point out that this cannot be expected in general; see [91, 14]. The computed

TABLE 10.1
Convergence rates for the 2D flower (top) and 3D popcorn (bottom) examples using $\mathbb{P}_1(\mathcal{T}_k)$.

Level k	$\\|e_k\\|_\Omega$	EOC	$\frac{1}{\sqrt{2}}\\||b\cdot n|^{1/2}[e_k]\\|_{\mathcal{F}_h}$	EOC	$\\|\phi^{1/2} b\cdot\nabla e_k\\|_\Omega$	EOC
0	$8.69\cdot 10^{-3}$	–	$1.17\cdot 10^{-2}$	–	$1.82\cdot 10^{-2}$	–
1	$2.05\cdot 10^{-3}$	2.09	$3.91\cdot 10^{-3}$	1.58	$4.76\cdot 10^{-3}$	1.93
2	$5.25\cdot 10^{-4}$	1.96	$1.30\cdot 10^{-3}$	1.59	$1.64\cdot 10^{-3}$	1.53
3	$1.34\cdot 10^{-4}$	1.97	$4.44\cdot 10^{-4}$	1.55	$5.40\cdot 10^{-4}$	1.60
4	$3.33\cdot 10^{-5}$	2.01	$1.56\cdot 10^{-4}$	1.51	$2.02\cdot 10^{-4}$	1.42
5	$8.40\cdot 10^{-6}$	1.98	$5.42\cdot 10^{-5}$	1.52	$6.89\cdot 10^{-5}$	1.55
Level k	$\frac{1}{\sqrt{2}}\\||b\cdot n|^{1/2} e_k\\|_\Gamma$	EOC	$\\|e_k\\|_{L^2(\Gamma)}$	EOC	$\\|e_k\\|_{L^\infty(\Omega)}$	EOC
0	$1.20\cdot 10^{-2}$	–	$2.55\cdot 10^{-2}$	–	$4.29\cdot 10^{-2}$	–
1	$2.51\cdot 10^{-3}$	2.26	$4.74\cdot 10^{-3}$	2.43	$7.64\cdot 10^{-3}$	2.49
2	$7.00\cdot 10^{-4}$	1.84	$1.26\cdot 10^{-3}$	1.91	$3.43\cdot 10^{-3}$	1.15
3	$1.80\cdot 10^{-4}$	1.96	$3.34\cdot 10^{-4}$	1.92	$1.24\cdot 10^{-3}$	1.47
4	$4.51\cdot 10^{-5}$	1.99	$8.81\cdot 10^{-5}$	1.92	$3.16\cdot 10^{-4}$	1.97
5	$1.14\cdot 10^{-5}$	1.99	$2.29\cdot 10^{-5}$	1.94	$1.03\cdot 10^{-4}$	1.62

Level k	$\\|e_k\\|_\Omega$	EOC	$\frac{1}{\sqrt{2}}\\||b\cdot n|^{1/2}[e_k]\\|_{\mathcal{F}_h}$	EOC	$\\|\phi^{1/2} b\cdot\nabla e_k\\|_\Omega$	EOC
0	$1.86\cdot 10^{-2}$	–	$1.82\cdot 10^{-2}$	–	$3.48\cdot 10^{-2}$	–
1	$4.41\cdot 10^{-3}$	2.07	$7.35\cdot 10^{-3}$	1.31	$1.10\cdot 10^{-2}$	1.66
2	$1.07\cdot 10^{-3}$	2.05	$2.58\cdot 10^{-3}$	1.51	$3.11\cdot 10^{-3}$	1.83
3	$2.62\cdot 10^{-4}$	2.02	$8.29\cdot 10^{-4}$	1.64	$1.11\cdot 10^{-3}$	1.49
4	$6.54\cdot 10^{-5}$	2.00	$2.73\cdot 10^{-4}$	1.60	$3.54\cdot 10^{-4}$	1.65
Level k	$\frac{1}{\sqrt{2}}\\||b\cdot n|^{1/2} e_k\\|_\Gamma$	EOC	$\\|e_k\\|_{L^2(\Gamma)}$	EOC	$\\|e_k\\|_{L^\infty(\Omega)}$	EOC
0	$1.75\cdot 10^{-2}$	–	$3.74\cdot 10^{-2}$	–	$4.55\cdot 10^{-2}$	–
1	$4.62\cdot 10^{-3}$	1.92	$9.17\cdot 10^{-3}$	2.03	$1.27\cdot 10^{-2}$	1.84
2	$1.18\cdot 10^{-3}$	1.97	$2.34\cdot 10^{-3}$	1.97	$3.94\cdot 10^{-3}$	1.69
3	$3.02\cdot 10^{-4}$	1.96	$6.17\cdot 10^{-4}$	1.92	$1.15\cdot 10^{-3}$	1.77
4	$7.70\cdot 10^{-5}$	1.97	$1.65\cdot 10^{-4}$	1.90	$3.63\cdot 10^{-4}$	1.67

convergence rate orders using the $\|\cdot\|_\Gamma$ and $\|\cdot\|_{L^\infty}$ norms are close to 2 and 1.5, respectively.

Finally, we repeat the numerical experiment with $\mathbb{P}_0$ elements, but this time, we disable any ghost penalty stabilization. The resulting errors for the 2D flower domain are reported in Table 10.2, with rates between $\mathcal{O}(h^{1/2})$ and $\mathcal{O}(h)$, confirming the convergence rates predicted by Proposition 6.3. The experimentally observed convergence rates for the 3D popcorn domain were very similar and are not reported here.

10.1.2. Wavy inflow and outflow boundary. Next, we study the performance of the proposed CutDG method using high-order elements for smooth solutions and at the presence of a sharp internal layer in the manufactured solution. To cover both scenarios within a single problem setup, we manufacture an analytical solution u_ϵ depending on a parameter ϵ which results in a smooth function if $\epsilon \sim 1$, while choosing $\epsilon \ll 1$ produces a solution with a sharp internal layer. In the latter case, the manufactured solution is practically discontinuous whenever the internal layer cannot be resolved by the mesh. In both test cases, the problem (2.1) is solved on the domain

$$\Omega = [-1.0, 1.0]^2 \cap \{\phi^+ < 0.85\} \cap \{\phi^- > -0.85\}, \tag{10.6}$$

TABLE 10.2
Convergence rates for the 2D flower example using $\mathbb{P}_0(\mathcal{T}_k)$.

Level N	$\\|e_k\\|_\Omega$	EOC	$\frac{1}{\sqrt{2}}\\||b\cdot n|^{1/2}[e_k]\\|_{\mathcal{F}_h}$	EOC	$\\|\phi^{1/2} b\cdot\nabla e_k\\|_\Omega$	EOC
0	$5.43\cdot 10^{-2}$	–	$1.37\cdot 10^{-1}$	–	$2.08\cdot 10^{-1}$	–
1	$3.27\cdot 10^{-2}$	0.73	$1.04\cdot 10^{-1}$	0.40	$1.37\cdot 10^{-1}$	0.61
2	$1.60\cdot 10^{-2}$	1.03	$7.65\cdot 10^{-2}$	0.45	$9.22\cdot 10^{-2}$	0.57
3	$8.38\cdot 10^{-3}$	0.93	$5.42\cdot 10^{-2}$	0.50	$6.28\cdot 10^{-2}$	0.55
4	$4.13\cdot 10^{-3}$	1.02	$3.86\cdot 10^{-2}$	0.49	$4.52\cdot 10^{-2}$	0.47
5	$2.19\cdot 10^{-3}$	0.91	$2.73\cdot 10^{-2}$	0.50	$3.10\cdot 10^{-2}$	0.55
Level k	$\frac{1}{\sqrt{2}}\\||b\cdot n|^{1/2}e_k\\|_\Gamma$	EOC	$\\|e_k\\|_{L^2(\Gamma)}$	EOC	$\\|e_k\\|_{L^\infty(\Omega)}$	EOC
0	$9.87\cdot 10^{-2}$	–	$2.03\cdot 10^{-1}$	–	$3.12\cdot 10^{-1}$	–
1	$6.03\cdot 10^{-2}$	0.71	$1.21\cdot 10^{-1}$	0.74	$2.21\cdot 10^{-1}$	0.50
2	$2.87\cdot 10^{-2}$	1.07	$5.41\cdot 10^{-2}$	1.16	$1.01\cdot 10^{-1}$	1.13
3	$1.54\cdot 10^{-2}$	0.90	$3.17\cdot 10^{-2}$	0.77	$7.17\cdot 10^{-2}$	0.49
4	$7.87\cdot 10^{-3}$	0.97	$1.77\cdot 10^{-2}$	0.84	$4.81\cdot 10^{-2}$	0.58
5	$4.10\cdot 10^{-3}$	0.94	$9.88\cdot 10^{-3}$	0.84	$2.64\cdot 10^{-2}$	0.87

where

$$\phi^+(x,y) = y - 0.1\cos(8x), \qquad \phi^-(x,y) = y + 0.1\cos(8x). \tag{10.7}$$

The velocity field b and the analytical solution u_ϵ are set to

$$\begin{aligned} u_\epsilon(x,y) &= \exp(\lambda(x,y)\arcsin((1-x^2)\pi\cos(2\pi y)/25))\arctan(\lambda(x,y)/\epsilon),\\ b(x,y) &= ((1-x^2)\pi\cos(2\pi y)/25, (1+4x^2)/5), \end{aligned} \tag{10.8}$$

where $\lambda(x,y) = (x - 0.1\sin(2\pi y))/5$. It is also important to realize that λ defines the shape of the internal layer. Thanks to the definition of the velocity field b, we observe that the inflow and outflow boundaries are defined by the level sets

$$\Gamma^- = \{\phi^- = -0.85\}\cap\Omega, \qquad \Gamma^+ = \{\phi^+ = 0.85\}\cap\Omega, \tag{10.9}$$

and for $\epsilon \ll 1$, the streamlines of the velocity field b are parallel to the discontinuity; see Figure 10.2 (bottom). For our convergence tests, we study two extreme cases where we set $\epsilon = 1.0$ first and $\epsilon = 10^{-8}$ later. Recalling the a priori error analysis from section 6, the expected convergence rate for smooth solutions is $\mathcal{O}(h^{p+1/2})$. For the discontinuous case, one can only expect a convergence order of at most $\mathcal{O}(h^{1/2})$ in the (global) L^2 norm, independently of the chosen polynomial order p. Consequently, we consider only the case $p = 1$ for the nearly discontinuous solution.

Now setting $\epsilon = 1$ in (10.8), we obtain a smooth solution; see Figure 10.2 (left). Employing high-order elements up to $p = 3$, optimal convergence rates are obtained; see Figure 10.3. As before, we observe an EOC of $\mathcal{O}(h^{p+1})$ rather than $\mathcal{O}(h^{p+1/2})$ in the L^2 norm. Next, we set $\epsilon = 10^{-8}$ in (10.8), where we observe a sharp internal layer in the middle of the domain; see Figure 10.2 (right). For our mesh resolution, this layer can be considered as discontinuous and the tabulated results in Table 10.3 (top) confirm the reduction of the convergence order to $\mathcal{O}(h^{1/2})$ in the L^2 norm, and with no convergence in the other considered error norms. A closer look at the computed solution in Figure 10.2 (right) shows the typical oscillations triggered by the Gibbs phenomenon which, as in the standard fitted upwind DG method, only appear in the close vicinity of the layer. For completeness, we repeat the numerical experiment but

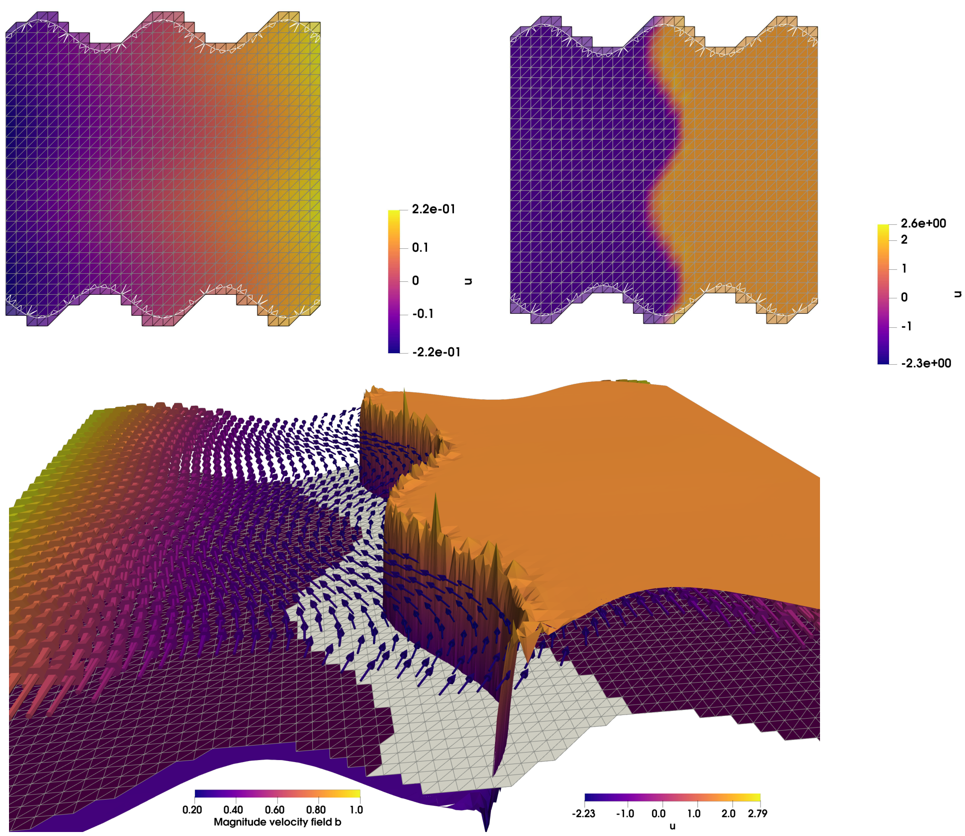

FIG. 10.2. *Solution plots for wavy inflow and outflow boundary example. (Top left) Smooth solution with $\epsilon = 1$. (Top right) Nearly discontinuous solution with $\epsilon = 10^{-8}$. In both cases the solution is plotted over the active background mesh $\mathcal{T}_k$; the wavy inflow and outflow boundaries together with the physical domain are shown as well. (Bottom) Close-up of the graph of the computed approximation to the rough solution near the discontinuity, together with the velocity field b. Gray mesh domain around the discontinuity was disregarded in modified EOC computations, where only the error away from the internal layer was considered.*

this time, we confine the error computations to those elements and faces which are contained in $\Omega_\delta = \Omega \setminus \{(x, y) \in \mathbb{R}^2 \mid |\lambda(x, y)| > 5\delta\}$ with $\delta = 0.25$. The exclusion of a δ tubular neighborhood around the sharp layer restores the previous optimal convergence rates as indicated by results displayed in Table 10.3 (bottom). How to combine the proposed stabilized CutDG framework with various shock capturing or limiter techniques [101] to control spurious oscillation near discontinuities will be part of our future research.

10.2. Geometrical robustness. Further, we numerically investigate the geometrical robustness of the derived a priori error and condition number estimates, illustrating the importance and different roles of the ghost penalties g_c and g_b. Our experiments are based on the following setup. We start from a structured background mesh $\widetilde{\mathcal{T}}_h$ for the rectangular domain $\widetilde{\Omega} = [-0.35, 0.35]^2 \subset \mathbb{R}^2$ with mesh size $h = 0.7/N$ and $N = 10$. To generate potentially critical cut configurations, we define a family $\{\Omega_{\delta_k}\}_{k=1}^{1000}$ of translated circular domains $\Omega_{\delta_k} = \Omega + \delta_k \boldsymbol{t}$ with initial domain $\Omega = \{(x, y) \in \mathbb{R}^2 \mid x^2 + y^2 - 0.25^2 < 0\}$ and set the translation vector $\boldsymbol{t}$ and translation parameter δ_k to $\frac{1}{\sqrt{2}}(h, h)$ and $k/1000$, respectively.

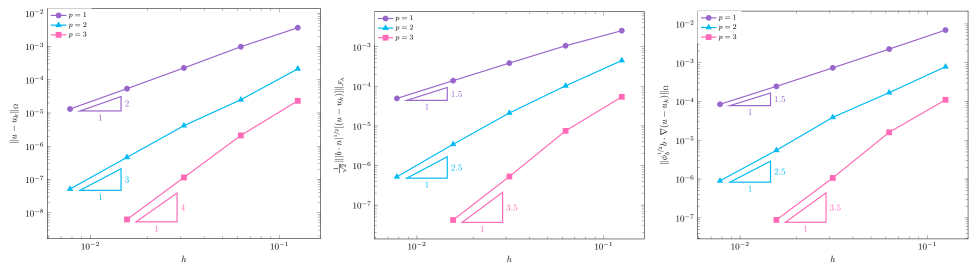

(a) Convergence rates in the $L^2(\Omega)$ (left), upwind flux (middle), and streamline diffusion (right) norms.

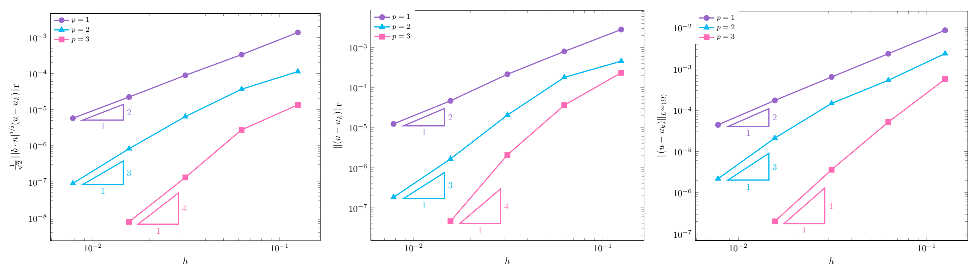

(b) Convergence rates in the weighted $L^2(\Gamma)$ (left), standard $L^2(\Gamma)$ (middle), and $L^\infty(\Omega)$ (right) norms.

FIG. 10.3. *Observed error convergence rates for wavy inflow and outflow example with $p = 1, 2, 3$. For $p = 3$, computer memory restrictions prohibited performing more than three mesh refinements.*

TABLE 10.3

Convergence rates for the third example with a sharp internal layer for $\epsilon = 10^{-8}$ using $\mathbb{P}_1(\mathcal{T}_k)$. Error norms are computed on the whole domain (top) and outside a δ neighborhood of the transition layer with $\delta = 0.25$ (bottom).

Level k	$\|e_k\|_\Omega$	EOC	$\frac{1}{\sqrt{2}}\||b\cdot n|^{1/2}[e_k]\|_{\mathcal{F}_h}$	EOC	$\|\phi^{1/2}b\cdot\nabla e_k\|_\Omega$	EOC
0	$8.68\cdot10^{-1}$	–	$1.30\cdot10^{-1}$	–	$9.05\cdot10^{-1}$	–
1	$5.83\cdot10^{-1}$	0.57	$1.31\cdot10^{-1}$	−0.01	$1.12\cdot10^{0}$	−0.31
2	$4.05\cdot10^{-1}$	0.52	$1.27\cdot10^{-1}$	0.04	$1.08\cdot10^{0}$	0.06
3	$2.83\cdot10^{-1}$	0.52	$9.80\cdot10^{-2}$	0.37	$1.00\cdot10^{0}$	0.10
4	$2.14\cdot10^{-1}$	0.40	$7.52\cdot10^{-2}$	0.38	$1.00\cdot10^{0}$	0.00
Level k	$\|e_k\|_\Omega$	EOC	$\frac{1}{\sqrt{2}}\||b\cdot n|^{1/2}[e_k]\|_{\mathcal{F}_h}$	EOC	$\|\phi^{1/2}b\cdot\nabla e_k\|_\Omega$	EOC
0	$6.96\cdot10^{-1}$	–	$1.06\cdot10^{-1}$	–	$8.15\cdot10^{-1}$	–
1	$3.10\cdot10^{-2}$	4.49	$2.25\cdot10^{-2}$	2.24	$1.49\cdot10^{-2}$	5.77
2	$3.78\cdot10^{-4}$	6.36	$5.32\cdot10^{-4}$	5.40	$9.61\cdot10^{-4}$	3.95
3	$7.62\cdot10^{-5}$	2.31	$1.71\cdot10^{-4}$	1.64	$2.98\cdot10^{-4}$	1.69
4	$1.87\cdot10^{-5}$	2.03	$6.05\cdot10^{-5}$	1.50	$1.01\cdot10^{-4}$	1.56

10.2.1. Sensitivity of the approximation error. In our first robustness test, we compute the $\|\cdot\|_\Omega$ and $\|\phi_b^{1/2} b\cdot\nabla(\cdot)\|_\Omega$ errors of the method (3.9) as a function of the translation parameter δ. The manufactured solution, velocity field, and reaction term are again given by (10.3). To demonstrate that the ghost penalties are necessary to render the errors insensitive to the particular cut configuration, we repeat the computation with either g_c or g_b or with both turned off, setting the corresponding

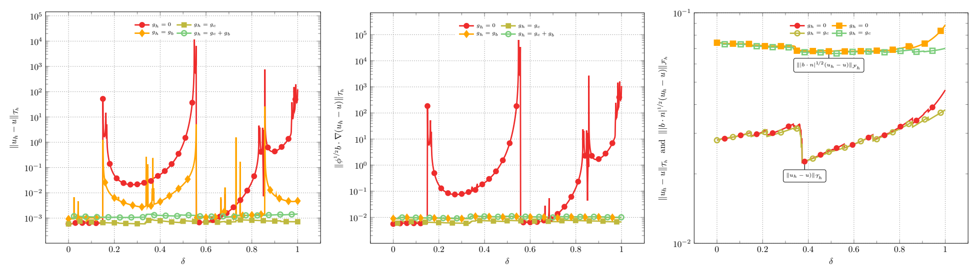

FIG. 10.4. *Error sensitivity for different choices of g_h in the translated domain test considering $\mathbb{P}_1(\mathcal{T}_h)$ and $\mathbb{P}_0(\mathcal{T}_h)$ spaces for various norms. (Left) L^2 error sensitivity for $\mathbb{P}_1(\mathcal{T}_h)$. (Middle) Streamline diffusion error sensitivity for $\mathbb{P}_1(\mathcal{T}_h)$. (Right) For $\mathbb{P}_0(\mathcal{T}_h)$, the L^2 and streamline diffusion error sensitivities are nearly unaffected by the absence of g_c.*

stabilization parameters to 0. The resulting plots displayed in Figure 10.4 show that both the $\|\cdot\|_\Omega$ and $\|\phi_b^{1/2} b\cdot\nabla(\cdot)\|_\Omega$ error curves are highly erratic and exhibit large spikes when the ghost penalties are completely turned off. For the fully stabilized method, on the other hand, the errors are largely insensitive to the translation parameter δ. We also observe that the L^2 error already appears to be geometrically robust when only g_c is activated, while the sole activation of g_b does not have such an effect. For the streamline diffusion error, both g_b and g_c have a stabilizing effect for the particular example. The stabilizing effect of g_c can be easily explained by recalling the definition of the unified ghost penalty g_h (cf. (8.19)), and realizing that for the given coefficients and considered coarse mesh size, we have that $c_0 \sim \frac{b_c}{h}$.

10.2.2. Sensitivity of the conditioning number. Using the identical setup as in section 10.2.1, we now compute the condition number of the system matrix (7.1) as a function of the translation parameter δ. For the fully stabilized formulation with stabilization parameters $\beta = \gamma_0 = \gamma_1 = 0.01$, we see that the condition number changes very mildly with the position parameter δ, while for the unstabilized formulation, large spikes can be observed up to the point where the system matrix is practically singular. In a second run, we study the effect of the magnitude of the ghost penalty parameters on the magnitude and geometrical robustness of the condition number. For simplicity, we rescale all ghost penalty parameters simultaneously. Figure 10.5 (right) shows that both the baseline magnitude and the fluctuation of the condition number decrease with increasing size of the stability parameters with a minimum for some $\gamma_b^f = \gamma_c^f \in [0.01, 1]$. A further increase of the stability parameters leaves the condition number insensitive to δ but leads to an increase of the overall magnitude. Combined with a series of convergence experiments (not presented here) for various parameter choices and combinations, we found that our parameter choice $\gamma_b^f = \gamma_b^c = 0.01$ offers a good balance between the accuracy of the numerical scheme and the magnitude and fluctuation of the condition number.

10.3. Time-dependent problem. We now briefly demonstrate solving the time-dependent problem (2.8) using the fully discretized schemes (9.3) and (9.4). The library deal.II [1] was used to implement and conduct the numerical experiments in this section. Here, the face-based stabilization is used for M_h ((3.14), (3.15), and (8.2)) and the crosswind version of the ghost penalty (8.19) is used for A_h. Let Ω be a circular domain,

$$\Omega = \{x \in \mathbb{R}^2 \mid x_1^2 + x_2^2 - 0.25^2 < 0\}, \tag{10.10}$$

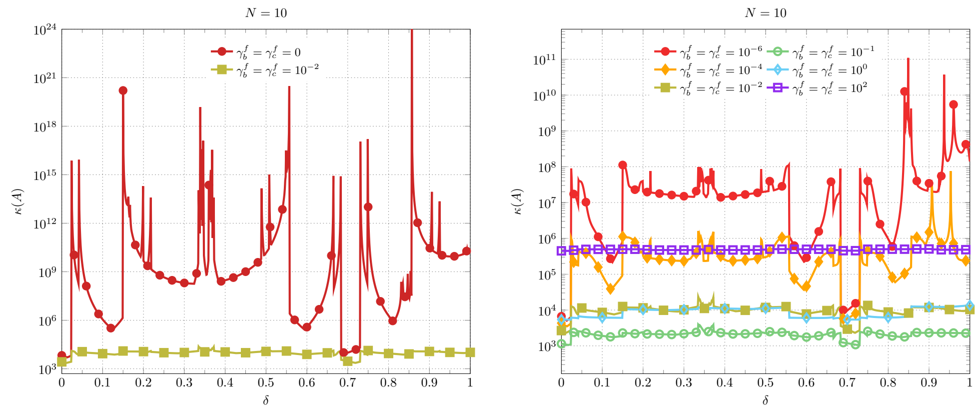

FIG. 10.5. *(Left) Condition number sensitivity for the translated domain test with and without ghost penalty stabilization g_c. (Right) Condition number sensitivity for changing values of the stabilization parameters γ_b^f and γ_c^f.*

covered by a quadrilateral background mesh over $\widetilde{\Omega} = [-0.35, 0.35]^2 \subset \mathbb{R}^2$. Let $b = (0.6, 0.8)$ and $c = 1$ be constant. We consider the manufactured solution

$$u(x,t) = \Theta(x - bt), \tag{10.11}$$

where $\Theta : \mathbb{R}^2 \to \mathbb{R}$ is a given function. This choice of u fulfills (2.8) with the data

$$f(x,t) = c\Theta(x - bt), \tag{10.12}$$

$$g(x,t) = \Theta(x - bt). \tag{10.13}$$

In the following experiment, we choose

$$\Theta(x) = \sum_i \cos(\omega x_i) \tag{10.14}$$

with $\omega = 8\pi$. We shall consider both Q_0 and Q_2 elements, i.e., tensor product Lagrange polynomials of order 0 and order 2 on quadrilateral elements. Let h_s denote the side length of the quadrilaterals ($h = \sqrt{2}h_s$). We solve until end time $T = 1$, with a time step

$$\Delta t = 0.1 h_s, \tag{10.15}$$

using the method (9.3) for Q_0 elements and (9.4) for Q_2 elements. A few snapshots of the numerical solution are shown in Figure 10.6.

Next, we perform a first convergence study where the mesh and time step are refined simultaneously. More detailed numerical experiments of the time-dependent case are beyond the scope of the present paper and will be presented elsewhere. We are interested in the error at $t = T$ in the L^2 norm and in the following seminorm:

$$|v|_b^2 = \frac{1}{2}\int_{\partial\Omega} |b \cdot n| v^2 + \frac{1}{2}\int_{\mathcal{F}_h} |b \cdot n| [v]^2. \tag{10.16}$$

Note that since we integrate over $\mathcal{F}_h$ in (10.16), this error is computed against the extension of the solution to $\mathcal{T}_h$. The errors for decreasing grid-sizes, $h_s = 0.7/40 \cdot 2^{-k}$,

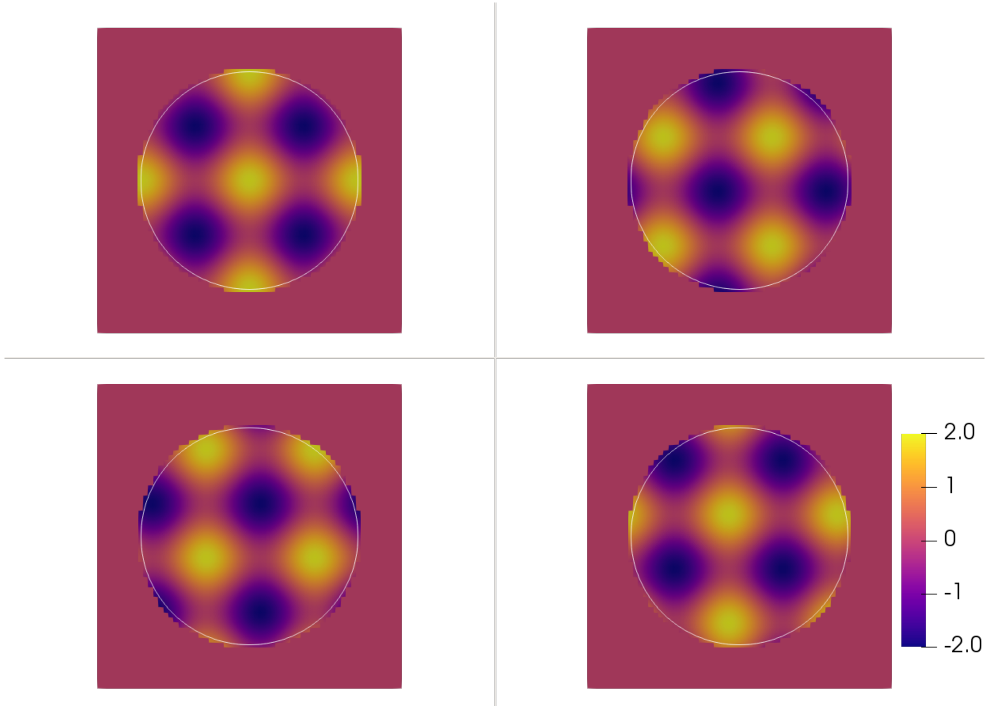

FIG. 10.6. *Snapshots of the solution to the problem from section* 10.3*, solved with* Q_2 *elements and* $h = 0.7/160$*. Top left,* $t = 0$*; top right,* $t = T/8$*; bottom left,* $t = T/4$*; bottom right,* $t = 3T/8$*.*

TABLE 10.4
Convergence rates for the time-dependent problem in section 10.3*.*

(a) Using Q_0 elements.

Level k	$\|e_k\|_\Omega$	EOC	$\|e_k\|_b$	EOC
0	$2.00 \cdot 10^{-1}$	–	0.60	–
1	$1.30 \cdot 10^{-1}$	0.68	0.49	0.27
2	$7.17 \cdot 10^{-2}$	0.81	0.39	0.36
3	$3.85 \cdot 10^{-2}$	0.90	0.29	0.42
4	$2.00 \cdot 10^{-2}$	0.95	0.21	0.46
5	$1.02 \cdot 10^{-2}$	0.97	0.15	0.48

(b) Using Q_2 elements.

Level k	$\|e_k\|_\Omega$	EOC	$\|e_k\|_b$	EOC
0	$6.27 \cdot 10^{-4}$	–	$9.38 \cdot 10^{-3}$	–
1	$5.90 \cdot 10^{-5}$	3.41	$1.17 \cdot 10^{-3}$	3.00
2	$6.12 \cdot 10^{-6}$	3.27	$1.67 \cdot 10^{-4}$	2.81
3	$6.29 \cdot 10^{-7}$	3.28	$2.48 \cdot 10^{-5}$	2.75

are shown in Table 10.4(a) for Q_0 elements and in Table 10.4(b) for Q_2 elements. We see that for Q_0 elements the error converges as $\mathcal{O}(h)$ in the L^2 norm and as $\mathcal{O}(h^{1/2})$ in the $|\cdot|_b$ seminorm. Furthermore, for Q_2 elements we see that the error converges at least as $\mathcal{O}(h^3)$ in the L^2 norm and at least as $\mathcal{O}(h^{5/2})$ in the $|\cdot|_b$ seminorm.

In the same manner as in section 10.2, we consider how the errors change when we perturb the domain. For a fixed grid of size $h_s = 0.7/N$, $N = 25$, we consider a family of translated domains $\Omega_{\delta_k} = \Omega + (\delta_k - \frac{1}{2})\boldsymbol{t}$, with $\boldsymbol{t} = (h, h)$ and $\delta_k = k/1001$, $k \in \{1, \dots, 1000\}$. The two error norms are shown in Figure 10.7 as a function of δ. We see that there is only a small variation in the error when we vary δ.

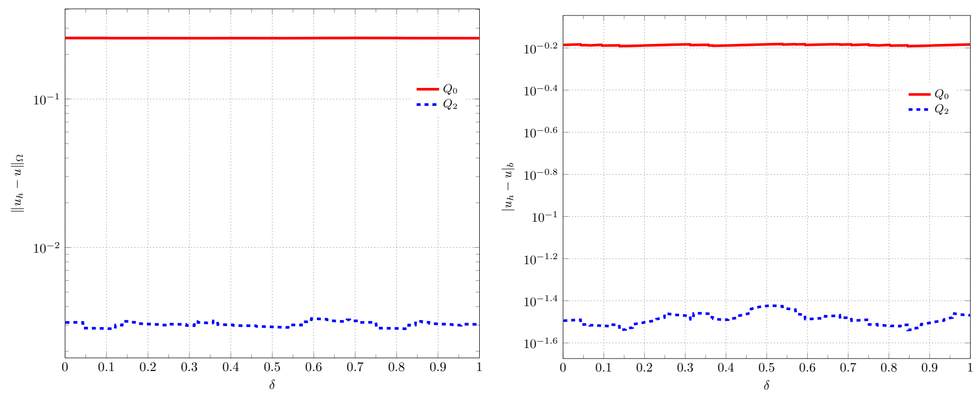

FIG. 10.7. *Error sensitivity for the translated domain test, for the time-dependent problem in section* 10.3. *Error in the L^2 norm (left) and the $|\cdot|_b$ seminorm (right).*

11. Conclusions and outlook. In this paper, we introduced and analyzed stabilized CutDG methods for advection-reaction problems, with a strong focus on stationary problems. By adding certain stabilization in the vicinity of the embedded boundary, we were able to prove geometrically robust optimal a priori error and condition number estimates which are not affected by the presence of small cut cells. Our approach works for higher-order DG methods and, avoiding more classical stabilization strategies such as cell merging, can be incorporated into typical DG software frameworks with relative ease. For the sake of simplicity, we assumed simplicial meshes in the theoretical analysis. However, similar to [61], the method directly generalizes to quadrilateral or hexahedral meshes, which we tested numerically in section 10.3. While the prototype problems (2.1) and (2.8) are already of importance in many applications, our long-term goal is to devise high-order CutDG methods for more complex simulation scenarios, including mixed-dimensional coupled problems, time-dependent linear hyperbolic problems, and nonlinear conservations laws on complicated or possibly evolving domains. We therefore conclude our presentation with a short outlook on natural prototype problems and challenges which need to be addressed in further developments of our CutDG method.

Regarding time-dependent problems, an additional major challenge in unfitted discretization methods is that the presence of small cut cells can lead to severe time-step restrictions in explicit time-stepping methods. To date, all unfitted DG methods and many finite volume based Cartesian cut cell methods address this problem via cell merging. Devising robust cell merging algorithms can be delicate for complex and in particular moving 3D domains and requires nontrivial adaptions of internal data structures. We think the method (3.13), where we stabilize the L^2 scalar product/mass matrix associated with the time derivative, is a promising alternative route. The resulting modified mass matrix is geometrically robust and thus expected to lead to similar time-step restrictions as its fitted counterparts. It is part of our ongoing research to combine the presented stabilized CutDG framework with the general symmetric stabilization approach proposed in [18] to devise an explicit Runge–Kutta method for first-order Friedrich type operators covering advection reaction problems as well as linear wave propagation phenomena.

For the numerical discretization of nonlinear scalar hyperbolic conservation laws it will be interesting to investigate how the proposed CutDG stabilization can be combined with the DG Runge–Kutta methods originally developed in [35, 34, 33, 32]. Here, an important ingredient will be to combine small cut cell related stabilizations with limiting techniques to achieve high-order accuracy for smooth solutions and, at the same time, ensure the computation of nonoscillatory, physically compatible approximations near discontinuities. This is in particular crucial when the discontinuity is located close to the embedded boundary as ghost penalty stabilizations are designed to be weakly consistent for *smooth* solutions. Without modifications, we expect that such a scheme can lead to nonphysical, entropy-violating solutions, similar to the failure of certain linear symmetric stabilization techniques; see [42]. For face-based ghost penalties, one possible approach might be then to extend the nonlinear weighting of face-based stabilization suggested in [42]. Another possible direction is to explore how CutDG stabilizations can be paired with limiters based on the weighted essentially nonoscillatory methodology which has been proposed for fitted DG methods rather recently; see [102] for a short survey and a comprehensive bibliography.

Finally, we want to mention that diffusion-convection-reaction problems in the form of mixed-dimensional coupled surface-bulk problems have drawn a lot of attention in recent years, as such problems occur naturally in, e.g., flow and transport problems in fractured porous media, transport of surface-active agents in immiscible two-phase flow systems, and the modeling of cell motility; see, e.g., [49, 63, 50, 81]. To discretize the resulting multiphysics systems on complex or moving domains, we plan to combine the presented CutDG method with results from our previous work on CutFEMs for surfaces and coupled surface-bulk problems [23, 25, 62, 82].

Acknowledgment. The authors wish to thank the anonymous referees for the careful reading of the manuscript and for the constructive comments and helpful suggestions, which helped us to improve the quality of this paper.

REFERENCES

[1] D. Arndt, W. Bangerth, T. C. Clevenger, D. Davydov, M. Fehling, D. Garcia-Sanchez, G. Harper, T. Heister, L. Heltai, M. Kronbichler, R. M. Kynch, M. Maier, J.-P. Pelteret, B. Turcksin, and D. Wells, *The* `deal`*.II library, version* 9.1, J. Numer. Math., 27 (2019), https://doi.org/10.1515/jnma-2019-0064.
[2] D. Arnold, *An interior penalty finite element method with discontinuous elements*, SIAM J. Numer. Anal., 19 (1982), pp. 742–760.
[3] D. Arnold, F. Brezzi, B. Cockburn, and L. Marini, *Unified analysis of discontinuous Galerkin methods for elliptic problems*, SIAM J. Numer. Anal., 39 (2002), pp. 1749–1779.
[4] S. Badia, F. Verdugo, and A. F. Martín, *The aggregated unfitted finite element method for elliptic problems*, Comput. Methods Appl. Mech. Engrg., 336 (2018), pp. 533–553.
[5] P. Bastian and C. Engwer, *An unfitted finite element method using discontinuous Galerkin*, Internat. J. Numer. Methods Engrg, 79 (2009), pp. 1557–1576.
[6] P. Bastian, C. Engwer, J. Fahlke, and O. Ippisch, *An unfitted discontinuous Galerkin method for pore-scale simulations of solute transport*, Math. Comput. Simul., 81 (2011), pp. 2051–2061.
[7] R. Becker, E. Burman, and P. Hansbo, *A Nitsche extended finite element method for incompressible elasticity with discontinuous modulus of elasticity*, Comput. Methods Appl. Mech. Engrg., 198 (2009), pp. 3352–3360.
[8] M. Berger, *Cut cells: Meshes and solvers*, in Handbook of Numerical Analysis, Handb. Numer. Anal. 18, Elsevier, New York, 2017, pp. 1–22.
[9] M. Berger and C. Helzel, *A simplified h-box method for embedded boundary grids*, SIAM J. Sci. Comput., 34 (2012), pp. A861–A888.
[10] D. Boffi, N. Cavallini, and L. Gastaldi, *The finite element immersed boundary method with distributed lagrange multiplier*, SIAM J. Numer. Anal., 53 (2015), pp. 2584–2604.
[11] D. Boffi and L. Gastaldi, *A finite element approach for the immersed boundary method*, Comput. Struct., 81 (2003), pp. 491–501.

[12] S. Bordas, E. Burman, M. Larson, and M. Olshanskii, eds., *Geometrically Unfitted Finite Element Methods and Applications*, Springer, New York, 2018.
[13] F. Brezzi, L. D. Marini, and E. Süli, *Discontinuous galerkin methods for first-order hyperbolic problems*, Math. Models Methods Appl. Sci., 14 (2004), pp. 1893–1903.
[14] E. Burman, *A unified analysis for conforming and nonconforming stabilized finite element methods using interior penalty*, SIAM J. Numer. Anal., 43 (2005), pp. 2012–2033.
[15] E. Burman, *Ghost penalty*, C. R. Math., 348 (2010), pp. 1217–1220.
[16] E. Burman, S. Claus, P. Hansbo, M. G. Larson, and A. Massing, *CutFEM: Discretizing geometry and partial differential equations*, Internat. J. Numer. Methods Engng., 104 (2015), pp. 472–501.
[17] E. Burman, S. Claus, and A. Massing, *A stabilized cut finite element method for the three field Stokes problem*, SIAM J. Sci. Comput., 37 (2015), pp. A1705–A1726.
[18] E. Burman, A. Ern, and M. A. Fernández, *Explicit Runge–Kutta schemes and finite elements with symmetric stabilization for first-order linear pde systems*, SIAM J. Numer. Anal., 48 (2010), pp. 2019–2042.
[19] E. Burman, J. Guzmán, M. A. Sánchez, and M. Sarkis, *Robust flux error estimation of an unfitted nitsche method for high-contrast interface problems*, IMA J. Numer. Anal., 38 (2018), pp. 646–668.
[20] E. Burman and P. Hansbo, *Fictitious domain finite element methods using cut elements:* I. *A stabilized Lagrange multiplier method*, Comput. Methods Appl. Mech. Engrg., 199 (2010), pp. 2680–2686.
[21] E. Burman and P. Hansbo, *Fictitious domain finite element methods using cut elements:* II. *A stabilized Nitsche method*, Appl. Numer. Math., 62 (2012), pp. 328–341.
[22] E. Burman and P. Hansbo, *Fictitious domain methods using cut elements:* III. *A stabilized Nitsche method for Stokes' problem*, ESAIM Math. Model. Numer. Anal., 48 (2014), pp. 859–874.
[23] E. Burman, P. Hansbo, M. Larson, K. Larsson, and A. Massing, *Finite element approximation of the Laplace–Beltrami operator on a surface with boundary*, Numer. Math., 141 (2018), pp. 141–172.
[24] E. Burman, P. Hansbo, M. Larson, and S. Zahedi, *Cut finite element methods for coupled bulk-surface problems*, Numer. Math., 133 (2016), pp. 203–231.
[25] E. Burman, P. Hansbo, M. G. Larson, and A. Massing, *A cut discontinuous Galerkin method for the Laplace–Beltrami operator*, IMA J. Numer. Anal., 37 (2016), pp. 138–169.
[26] E. Burman, P. Hansbo, M. G. Larson, A. Massing, and S. Zahedi, *A Stabilized Cut Streamline Diffusion Finite Element Method for Convection-Diffusion Problems on Surfaces*, https://arxiv.org/abs/1807.01480, 2018.
[27] E. Burman, P. Hansbo, M. G. Larson, and S. Zahedi, *Stabilized CutFEM for the Convection Problem on Surfaces*, preprint, https://arxiv.org/abs/1511.02340, 2015.
[28] E. Burman and P. Zunino, *Numerical approximation of large contrast problems with the unfitted Nitsche method*, Front. Numer. Anal., 2010, (2012), pp. 1–54.
[29] L. Cattaneo, L. Formaggia, G. F. Iori, A. Scotti, and P. Zunino, *Stabilized extended finite elements for the approximation of saddle point problems with unfitted interfaces*, Calcolo, 52 (2015), pp. 123–152.
[30] D. K. Clarke, H. Hassan, and M. Salas, *Euler calculations for multielement airfoils using cartesian grids*, AIAA J., 24 (1986), pp. 353–358.
[31] B. Cockburn, *Discontinuous galerkin methods for convection-dominated problems*, in High-Order Methods for Computational Physics, Lect. Notes Comput. Sci. Eng. 9, Springer, New York, 1999, pp. 69–224.
[32] B. Cockburn, S. Hou, and C.-W. Shu, *The Runge-Kutta local projection discontinuous Galerkin finite element method for conservation laws.* IV. *The multidimensional case*, Math. Comp., 54 (1990), pp. 545–581.
[33] B. Cockburn, S.-Y. Lin, and C.-W. Shu, *TVB Runge-Kutta local projection discontinuous Galerkin finite element method for conservation laws.* III*: One-dimensional systems*, J. Comput. Phys., 84 (1989), pp. 90–113.
[34] B. Cockburn and C.-W. Shu, *TVB Runge-Kutta local projection discontinuous Galerkin finite element method for conservation laws.* II. *General framework*, Math. Comp., 52 (1989), pp. 411–435.
[35] B. Cockburn and C.-W. Shu, *The Runge-Kutta local projection-discontinuous-Galerkin finite element method for scalar conservation laws*, ESAIM Math. Model. Numer. Anal., 25 (1991), pp. 337–361.
[36] S. Court, M. Fournié, and A. Lozinski, *A fictitious domain approach for fluid-structure interactions based on the extended finite element method*, ESAIM Proc. Surveys, 45 (2014), pp. 308–317.

[37] C. D'Angelo and A. Scotti, *A mixed finite element method for Darcy flow in fractured porous media with non-matching grids*, ESAIM Math. Model. Numer. Anal., 46 (2012), pp. 465–489.
[38] D. A. Di Pietro and A. Ern, *Mathematical Aspects of Discontinuous Galerkin Methods*, Math. Appl. 69, Springer, New York, 2012.
[39] D. A. Di Pietro, A. Ern, and J.-L. Guermond, *Discontinuous Galerkin methods for anisotropic semidefinite diffusion with advection*, SIAM J. Numer. Anal., 46 (2008), pp. 805–831.
[40] A. Ern and J.-L. Guermond, *Discontinuous galerkin methods for Friedrichs' systems.* I. *General theory*, SIAM J. Numer. Anal., 44 (2006), pp. 753–778.
[41] A. Ern and J.-L. Guermond, *Evaluation of the condition number in linear systems arising in finite element approximations*, ESAIM Math. Model. Numer. Anal., 40 (2006), pp. 29–48.
[42] A. Ern and J.-L. Guermond, *Weighting the edge stabilization*, SIAM J. Numer. Anal., 51 (2013), pp. 1655–1677.
[43] F. Brezzi, G. Manzini, D. Marini, P. Pietra, and A. Russo, *Discontinuous Galerkin approximations for elliptic problems*, Numer. Methods Partial Differential Equations, 16 (2000), pp. 365–378.
[44] B. Flemisch, A. Fumagalli, and A. Scotti, *A review of the XFEM-based approximation of flow in fractured porous media*, in Advances in Discretization Methods: Discontinuities, Virtual Elements, Fictitious Domain Methods, SEMA SIMAI Springer Ser. 12, Springer, New York, 2016, pp. 47–76.
[45] L. Formaggia, A. Fumagalli, A. Scotti, and P. Ruffo, *A reduced model for Darcy's problem in networks of fractures*, ESAIM Math. Model. Numer. Anal., 48 (2013), pp. 1089–1116.
[46] T. Fries, S. Omerović, D. Schöllhammer, and J. Steidl, *Higher-order meshing of implicit geometriespart* I*: Integration and interpolation in cut elements*, Comput. Methods Appl. Mech. Engrg., 313 (2017), pp. 759–784.
[47] T.-P. Fries and S. Omerović, *Higher-order accurate integration of implicit geometries*, Internat. J. Numer. Methods Engrg., 106 (2016), pp. 323–371.
[48] A. Fumagalli, *Numerical Modelling of Flows in Fractured Porous Media by the XFEM Method*, Ph.D. thesis, Politecnico di Milano, Italy, 2012.
[49] A. Fumagalli and A. Scotti, *A numerical method for two-phase flow in fractured porous media with non-matching grids*, Adv. Water Resour., 62 (2013), pp. 454–464.
[50] S. Ganesan and L. Tobiska, *Arbitrary lagrangian–eulerian finite-element method for computation of two-phase flows with soluble surfactants*, J. Comput. Phys., 231 (2012), pp. 3685–3702.
[51] A. Gerstenberger and W. A. Wall, *An extended finite element method/Lagrange multiplier based approach for fluid–structure interaction*, Comput. Methods Appl. Mech. Engrg., 197 (2008), pp. 1699–1714.
[52] N. Gokhale, N. Nikiforakis, and R. Klein, *A dimensionally split cartesian cut cell method for hyperbolic conservation laws*, J. Comput. Phys., 364 (2018), pp. 186–208.
[53] S. Gross, T. Ludescher, M. Olshanskii, and A. Reusken, *Robust preconditioning for XFEM applied to time-dependent Stokes problems*, SIAM J. Sci. Comput., 38 (2016), pp. A3492–A3514.
[54] S. Gross, M. A. Olshanskii, and A. Reusken, *A trace finite element method for a class of coupled bulk-interface transport problems*, ESAIM Math. Model. Numer. Anal., 49 (2015), pp. 1303–1330.
[55] S. Gross, V. Reichelt, and A. Reusken, *A finite element based level set method for two-phase incompressible flows*, Comput. Vis. Sci., 9 (2006), pp. 239–257.
[56] S. Gross and A. Reusken, *Numerical Methods for Two-Phase Incompressible Flows*, Springer Ser. Comput. Math. 40, Springer, New York, 2011.
[57] C. Gürkan and A. Massing, *A Stabilized Cut Discontinuous Galerkin Framework:* I. *Elliptic Boundary Value and Interface Problems*, https://arxiv.org/abs/1803.06635, 2018.
[58] J. Guzmán and M. Olshanskii, *Inf-sup stability of geometrically unfitted Stokes finite elements*, Math. Comp., 87 (2018), pp. 2091–2112.
[59] J. Guzman, M. A. Sanchez, and M. Sarkis, *A Finite Element Method for High-Contrast Interface Problems with Error Estimates Independent of Contrast*, https://arxiv.org/abs/1507.03873, 2015
[60] A. Hansbo, P. Hansbo, and M. G. Larson, *A finite element method on composite grids based on Nitsche's method*, ESAIM Math. Model. Numer. Anal., 37 (2003), pp. 495–514.
[61] P. Hansbo, M. Larson, and K. Larsson, *Cut finite element methods for linear elasticity problems*, in Geometrically Unfitted Finite Element Methods and Applications, Springer, New York, 2017, pp. 25–63.

[62] P. Hansbo, M. G. Larson, and A. Massing, *A stabilized cut finite element method for the Darcy problem on surfaces*, Comput. Methods Appl. Math., 326 (2017), pp. 298–318.
[63] P. Hansbo, M. G. Larson, and S. Zahedi, *A cut finite element method for coupled bulk-surface problems on time-dependent domains*, Comput. Methods Appl. Mech. Engrg., 307 (2016), pp. 96–116.
[64] D. Hartmann, M. Meinke, and W. Schröder, *An adaptive multilevel multigrid formulation for cartesian hierarchical grid methods*, Comput. Fluids, 37 (2008), pp. 1103–1125.
[65] F. Heimann, C. Engwer, O. Ippisch, and P. Bastian, *An unfitted interior penalty discontinuous Galerkin method for incompressible Navier–Stokes two-phase flow*, Internat. J. Numer. Methods Fluids, 71 (2013), pp. 269–293.
[66] C. Helzel, M. J. Berger, and R. J. LeVeque, *A high-resolution rotated grid method for conservation laws with embedded geometries*, SIAM J. Sci. Comput., 26 (2005), pp. 785–809.
[67] J. S. Hesthaven and T. Warburton, *Nodal Discontinuous Galerkin Methods: Algorithms, Analysis, and Applications*, Springer, New York, 2007.
[68] P. Houston, C. Schwab, and E. Süli, *Stabilized hp-finite element methods for first-order hyperbolic problems*, SIAM J. Numer. Anal., 37 (2000), pp. 1618–1643.
[69] P. Houston, C. Schwab, and E. Süli, *Discontinuous hp-finite element methods for advection-diffusion-reaction problems*, SIAM J. Numer. Anal., 39 (2002), pp. 2133–2163.
[70] A. Johansson and M. Larson, *A high order discontinuous Galerkin Nitsche method for elliptic problems with fictitious boundary*, Numer. Math., 123 (2013), pp. 607–628.
[71] C. Johnson, U. Nävert, and J. Pitkäranta, *Finite element methods for linear hyperbolic problems*, Comput. Methods Appl. Mech. Engrg., 45 (1984), pp. 285–312.
[72] M. Kirchhart, S. Gross, and A. Reusken, *Analysis of an XFEM discretization for Stokes interface problems*, SIAM J. Sci. Comput., 38 (2016), pp. A1019–A1043.
[73] R. Klein, K. Bates, and N. Nikiforakis, *Well-balanced compressible cut-cell simulation of atmospheric flow*, Philos. Trans. A, 367 (2009), pp. 4559–4575.
[74] D. Krause and F. Kummer, *An incompressible immersed boundary solver for moving body flows using a cut cell discontinuous Galerkin method*, Comput. Fluids, 153 (2017), pp. 118–129.
[75] F. Kummer, *Extended discontinuous Galerkin methods for two-phase flows: The spatial discretization*, Internat. J. Numer. Methods Engrg., 109 (2017), pp. 259–289.
[76] C. Lehrenfeld, *High order unfitted finite element methods on level set domains using isoparametric mappings*, Comput. Methods Appl. Mech. Engrg., 300 (2016), pp. 716–733.
[77] P. Lesaint and P. Raviart, *On a finite element method for solving the neutron transport equation*, in Mathematical Aspects of Finite Elements in Partial Differential Equations, Academic Press, New York, 1974, pp. 89–123.
[78] J. Li, J. Melenk, B. Wohlmuth, and J. Zou, *Optimal a priori estimates for higher order finite elements for elliptic interface problems*, Appl. Numer. Math., 60 (2010), pp. 19–37.
[79] Z. Li and K. Ito, *The Immersed Interface Method: Numerical Solutions of PDEs Involving Interfaces and Irregular Domains*, Frontiers in Appl. Math. 33, SIAM, Philadelphia, 2006.
[80] Z. Li, T. Lin, and X. Wu, *New cartesian grid methods for interface problems using the finite element formulation*, Numer. Math., 96 (2003), pp. 61–98.
[81] W. Marth and A. Voigt, *Signaling networks and cell motility: A computational approach using a phase field description*, J. Math. Biol., (2013), pp. 1–22.
[82] A. Massing, *A cut discontinuous Galerkin method for coupled bulk-surface problems*, in Geometrically Unfitted Finite Element Methods and Applications, Lect. Notes Comput. Sci. Eng. 121, Springer, New York, 2017, pp. 259–279.
[83] A. Massing, M. Larson, A. Logg, and M. Rognes, *A stabilized Nitsche fictitious domain method for the Stokes problem*, J. Sci. Comput., 61 (2014), pp. 604–628.
[84] A. Massing, M. G. Larson, A. Logg, and M. Rognes, *A Nitsche-based cut finite element method for a fluid-structure interaction problem*, Commun. Appl. Math. Comput. Sci., 10 (2015), pp. 97–120.
[85] A. Massing, M. G. Larson, A. Logg, and M. E. Rognes, *A stabilized Nitsche overlapping mesh method for the Stokes problem*, Numer. Math., 128 (2014), pp. 73–101.
[86] A. Massing, B. Schott, and W. Wall, *A stabilized Nitsche cut finite element method for the Oseen problem*, Comput. Methods Appl. Mech. Engrg., 328 (2018), pp. 262–300.
[87] R. Massjung, *An unfitted discontinuous Galerkin method applied to elliptic interface problems*, SIAM J. Numer. Anal., 50 (2012), pp. 3134–3162.
[88] B. Müller, S. Krämer-Eis, F. Kummer, and M. Oberlack, *A high-order discontinuous Galerkin method for compressible flows with immersed boundaries*, Internat. J. Numer. Methods Engrg., 110 (2016), pp. 3–30. nme.5343.
[89] B. Müller, F. Kummer, and M. Oberlack, *Highly accurate surface and volume integration on implicit domains by means of moment-fitting*, Internat. J. Numer. Methods Engrg., 6 (2013), pp. 10–16.

[90] M. A. Olshanskii, A. Reusken, and X. Xu, *A stabilized finite element method for advection–diffusion equations on surfaces*, IMA J. Numer. Anal., 34 (2014), pp. 732–758.
[91] T. E. Peterson, *A note on the convergence of the discontinuous Galerkin method for a scalar hyperbolic equation*, SIAM J. Numer. Anal., 28 (1991), pp. 133–140.
[92] J. Preuss, *Higher Order Unfitted Isoparametric Space-Time FEM on Moving Domains*, Master's thesis, NAM, University of Göttingen, 2018.
[93] J. J. Quirk, *An alternative to unstructured grids for computing gas dynamic flows around arbitrarily complex two-dimensional bodies*, Comput. Fluids, 23 (1994), pp. 125–142.
[94] E. Rank, M. Ruess, S. Kollmannsberger, D. Schillinger, and A. Düster, *Geometric modeling, isogeometric analysis and the finite cell method*, Comput. Methods Appl. Mech. Engrg., 249 (2012), pp. 104–115.
[95] W. Reed and T. Hill, *Triangular Mesh Methods for the Neutron Transport Equation*, Technical Report LA-UR-73-479, Los Alamos Scientific Laboratory, Los Alamos, NM, 1973.
[96] R. Saye, *Implicit mesh discontinuous galerkin methods and interfacial gauge methods for high-order accurate interface dynamics, with applications to surface tension dynamics, rigid body fluid-structure interaction, and free surface flow: Part* i, J. Comput. Phys., 344 (2017), pp. 647–682.
[97] R. I. Saye, *High-order quadrature methods for implicitly defined surfaces and volumes in hyperrectangles*, SIAM J. Sci. Comput., 37 (2015), pp. A993–A1019.
[98] D. Schillinger and M. Ruess, *The finite cell method: A review in the context of higher-order structural analysis of CAD and image-based geometric models*, Arch. Comput. Methods Eng., 22 (2014), pp. 391–455.
[99] L. Schneiders, D. Hartmann, M. Meinke, and W. Schröder, *An accurate moving boundary formulation in cut-cell methods*, J. Comput. Phys., 235 (2013), pp. 786–809.
[100] B. Schott, U. Rasthofer, V. Gravemeier, and W. A. Wall, *A face-oriented stabilized Nitsche-type extended variational multiscale method for incompressible two-phase flow*, Internat. J. Numer. Methods Engrg., 104 (2015), pp. 721–748.
[101] C.-W. Shu, *High order weighted essentially nonoscillatory schemes for convection dominated problems*, SIAM Rev., 51 (2009), pp. 82–126.
[102] C.-W. Shu, *High order WENO and DG methods for time-dependent convection-dominated PDEs: A brief survey of several recent developments*, J. Comput. Phys., 316 (2016), pp. 598–613.
[103] W. E. H. Sollie, O. Bokhove, and J. J. W. van der Vegt, *Space–time discontinuous Galerkin finite element method for two-fluid flows*, J. Comput. Phys., 230 (2011), pp. 789–817.
[104] E. Stein, *Singular Integrals and Differentiability Properties of Functions*, Princeton University Press, Princeton, NJ, 1970.
[105] M. Winter, B. Schott, A. Massing, and W. Wall, *A Nitsche cut finite element method for the Oseen problem with general Navier boundary conditions*, Comput. Methods Appl. Mech. Engrg., 330 (2017), pp. 220–252.
[106] H. Zarin and H.-G. Roos, *Interior penalty discontinuous approximations of convection–diffusion problems with parabolic layers*, Numer. Math., 100 (2005), pp. 735–759.